

TITLE: Telescope Simulator optical design.

DISTRIBUTION

D Smith
B Swinyard
M Caldwell
T Grundy
M Ferlet
A Richards
M Harman
K Dohlen
P Hargrave
J Glenn

CHANGE RECORD

ISSUE	SECTION	REASON FOR CHANGE
1.0		first issue
2.0	All 8 & 9	update after RAL meeting (11/05/2001). re-visited verification budget (ref.5)
3.0	5 +Annex 2 & 3, 6, 8, 9 Annex 1	general update after SPIRE AIV DDR (06/09/2001) + update of interfaces. end of T. Grundy's Mphys project (Dec. 2001).

CONTENTS

Reference documents.

1. Introduction.
2. Simulator sizing.
3. Simulator (scanned) FOV.
4. SPIRE co-ordinate references.
5. Cryostat internal items.
 - 5.1. Cryostat window.
 - 5.2. Filter sizes.
6. Simulator & sources bench layout.
7. Pupil-scanned source.
8. Verification of SPIRE alignment (on simulator and STM).
9. Setting up the simulator.
10. Sources.

Annex 1. Telescope simulator control laws.

Annex 2. Filters & ghost reflections.

Annex 3. Flip-mirror & cryostat black body.

Annex 4. Beam patterns due to reflective pupil mask

Annex 5. Details of simulator bench layout.

Annex 6. Pupil scans alternative scheme.

Reference and applicable documents:

1. "Long wavelength (sub-mm) telescope simulator", W. Duncan et al., Infra-red Phys. Vol.34, No.1, pp.1-15 (1993).
2. MSSL interface drawing 5261: issue 11 (30-07-01)
3. SPIRE config. Spec04 & Phot03 .xls files.
4. SPIRE-RAL-NOT-000 621v4, "Design of the Telescope Simulator imaging mirror", M. Ferlet (3rd Dec. 01).
5. SPIRE optical error budgets LOOM.KD.SPIRE.2000.002 (5th Dec.00) + KD's e-mail 16-5-01.
6. SPIRE optical alignment + verification plan LOOM.KD.SPIRE.2000.001-3 (10th April.01)
7. SPIRE alignment tools specification LAM.PJT.SPI.SPT.20000x Ind. 0 (26th Oct.00).
8. SPIRE alignment sequence. Currently written as excel file of this name.
9. SPIRE telescope simulator facility requirements specification. SPIRE-RAL-PRJ-000463.

1. Introduction.

The purpose of the simulator is to provide a point-source beam at the instrument, of the form close to that from the Herschel telescope. This beam is one which is focused on the instrument FP surface, at the required f-number (8.7), and with a pupil distance equal to that of the telescope (approx. 2.64 metres, diameter ~ 300mm). The design concept is to use a single imaging optic as shown in fig.1, to produce the required pupil as a virtual image of a real stop, in order to save space as compared to using a real pupil. This concept was used for a UKIRT simulator (ref.1). For simplicity the imaging is made 1-to-1.

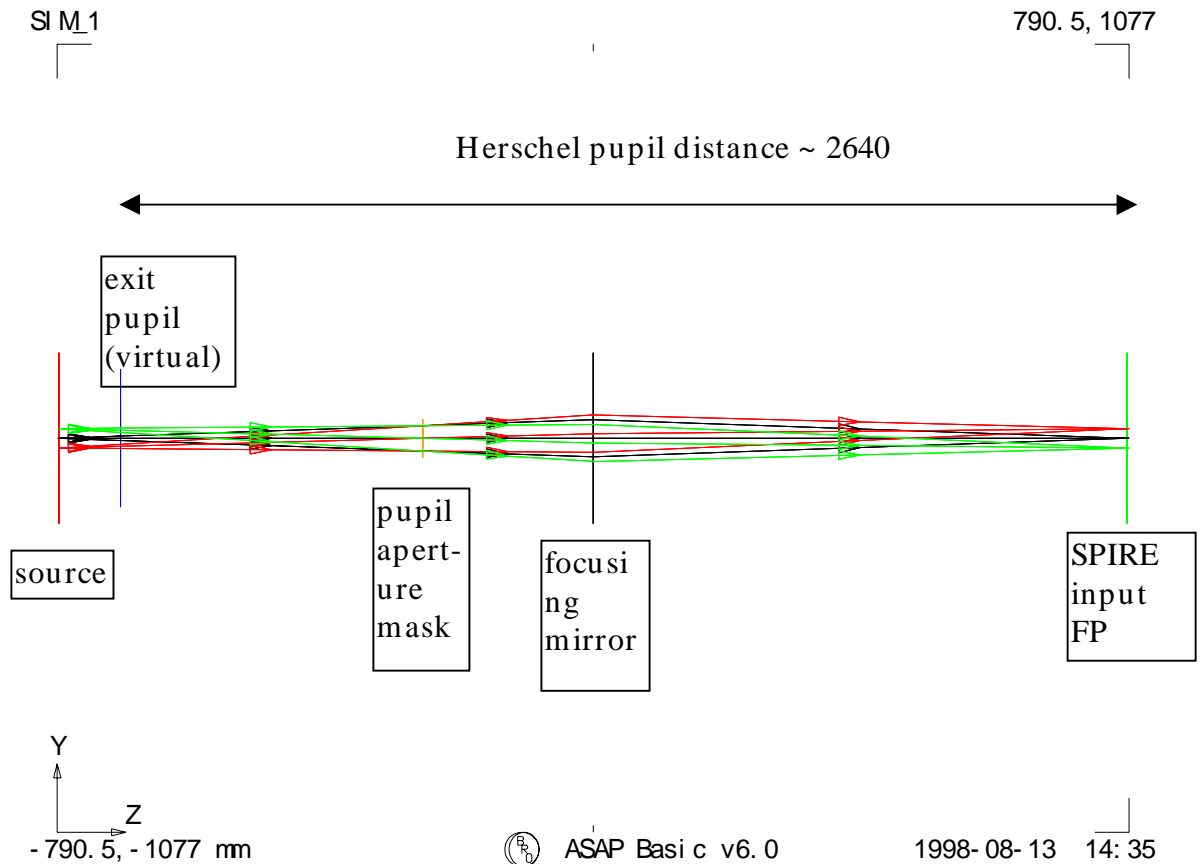


Fig.1. Simulator 1st-order layout, dimensions of plot window are as given at bottom-left & top-right corners (total length approx. 2 metres) Ray-trace is for geometric beam over used FOV.

Figure 1 shows a simulator used with an array of point sources, i.e. a finite FOV range, in order to show the pupil imagery. In practise, however, the need to keep the point-source aberration free over the SPIRE FOV range, and to keep the simulator imaging simple, leads to a design in which only one point source is imaged, and the FOV is mapped by scanning this beam after the imaging mirror.

In this scheme 3 fold mirrors are needed, and for an all-reflective implementation of the system of fig.1, we have a scheme as per fig.2. Here the imaging mirror is an ellipsoid with 90-degree turn angle, providing nominally perfect point source imaging.

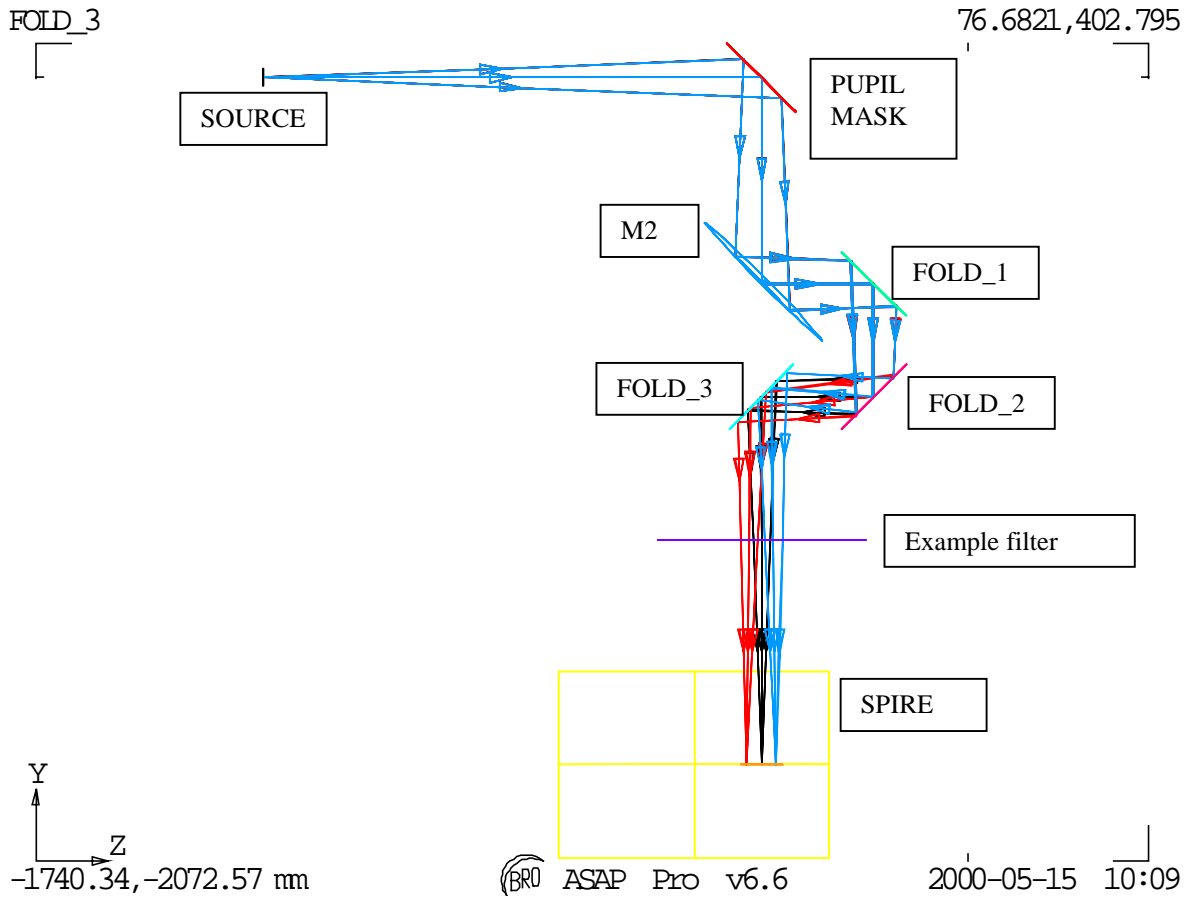


Fig.2. All-reflective design. Input point source shown in blue. The FOV scanning produces output beam also at FOV positions such as those shown in red & black.

Since the beam steering is all done after both the mask & the focusing mirror, so no changes in beam shape or aberration arise with scanning.

2. Simulator sizing.

Following ref.1, for accurate scaling in the representation of the larger (far-field) Herschel pupil the minimum beam dimension must be kept \gg wavelength, to maintain the far-field approximation. This dimension is the diameter D_{M1} of the mask's obscuration, & here we use $N \gg 1$ wavelengths, giving

$$D_{M1} = N * \lambda / \text{OBSC}$$

Where OBSC is the telescope obscuration factor, given by ratio of FIRST mirror sizes: D_{SM} / D_{PM} , and $\lambda = 0.6 \text{ mm}$.

The distance of the mask M1 from the source is

$$L_{M1} = D_{M1} * \text{FNO}$$

and FNO=8.7

And the required wavefront ROC produced by the 1:1 imaging mirror M2 is

$$R_{SM} = 2 * L_{M1} * L_{PUP} / (L_{M1} + L_{PUP})$$

$$L_{PUP} = (ROC_{SM} - \sqrt{(ROC_{SM}^2 - (K+1) * (D_{SM}/2)^2)}) / (K+1) + D_{SM-PM} + D_{PM-FP}$$

L_{PUP} is the pupil distance to be simulated (i.e. telescope system on-axis exit pupil position), and the 1st term in L_{PUP} is the approx. sag of the secondary mirror. For precise control L_{PUP} is later replaced by the off-axis position L'_{PUP} (section 3.2).

The parameter R_{SM} sets the overall size of the system. Note that the sizing may be changed by using imaging other than 1:1, but then a different FNO is required in the source.

The above figures give $R_{SM} \sim 2000$ mm, and to give an idea of scale the above simulator layout is shown overlaid with the Herschel telescope in fig.3 below.

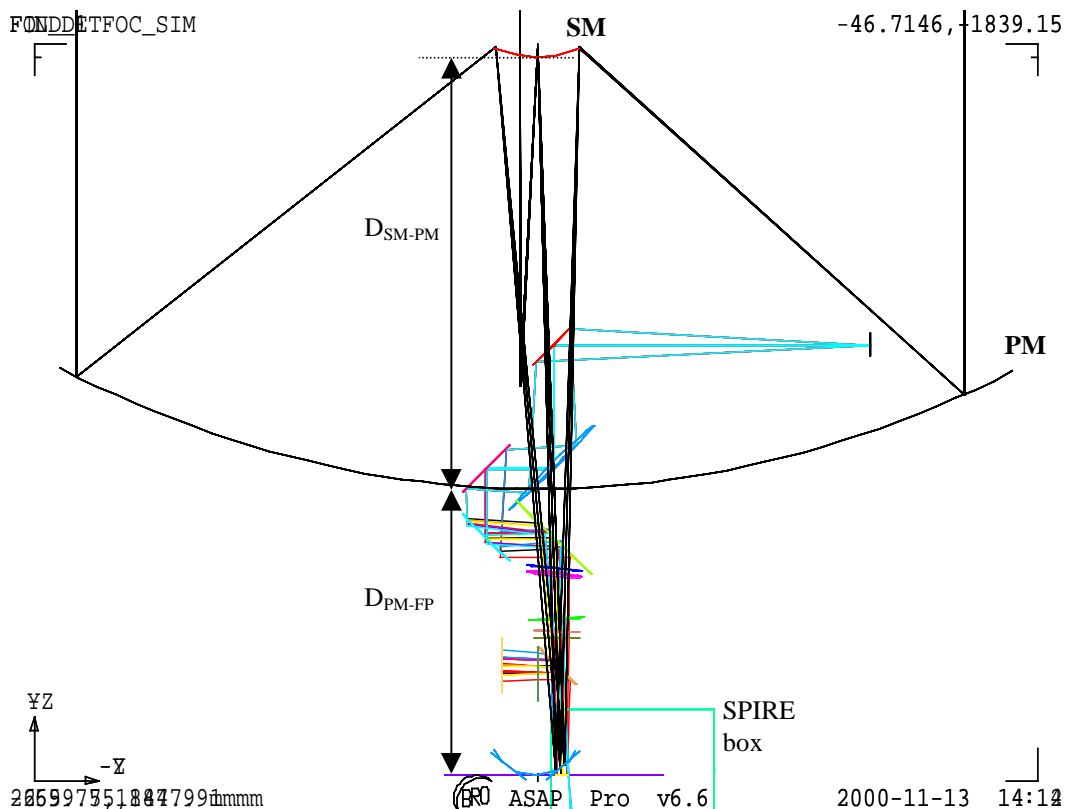


Fig.3. Simulator + Herschel systems overlaid.

The imaging mirror needed for this scheme has been investigated, to determine whether toroid or ellipsoid shape is preferred from the viewpoints of beam quality (aberration) requirement, alignment & manufacturing, and the size & spec. of this mirror. This study is reported in ref.4, and the conclusion is that an ellipsoidal shape is needed. Due to the large size this mirror cannot be made smooth & accurate enough to provide optical-quality imaging in the visible region. As a result the mirror verification & the alignment procedure will have to rely only on mechanical metrology, fiducial marks & small areas

of mirror polished. Also the simulator self-verification (of focus & steering control) will have to be performed at the SPIRE test wavelength (i.e. in FIR) ideally using e.g. a Golay cell detector, rather than with a visible trace beam as originally planned.

3. Simulator (scanned) FOV.

The simulator is required to cover the whole SPIRE instrument FOV without the need to re-configure any of the hardware within the cryostat.

The SPIRE geometric FOV is shown in the figure below.

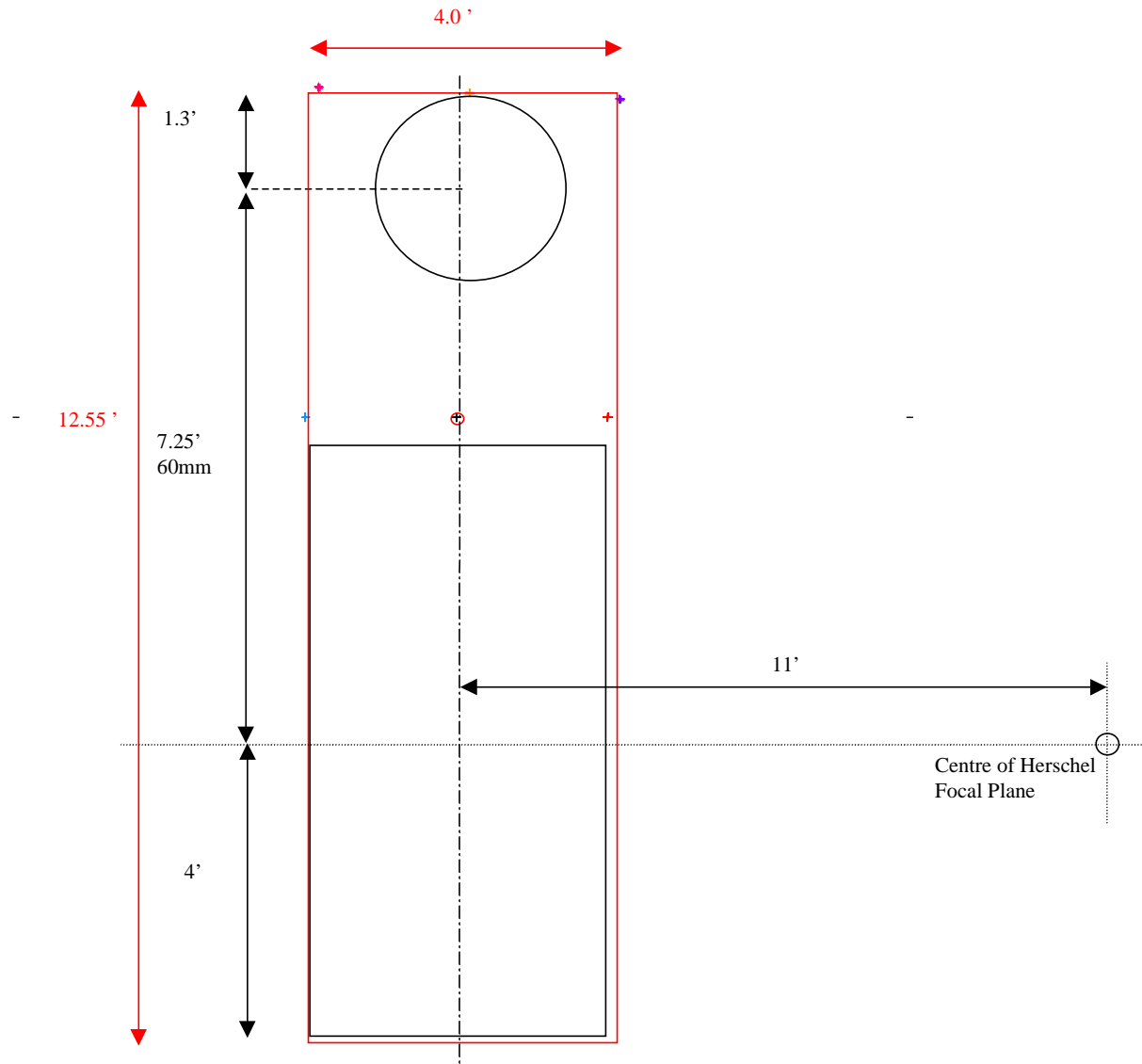


Fig.4. FOV simulator minimum FOV required is shown in red.

4. Spire co-ordinate references.

The off-axis location of the SPIRE FOV within the telescope FOV is by 11 arcmin, leading to 90mm offset of the SPIRE FP from the telescope symmetry axis, as shown in the fig. below.

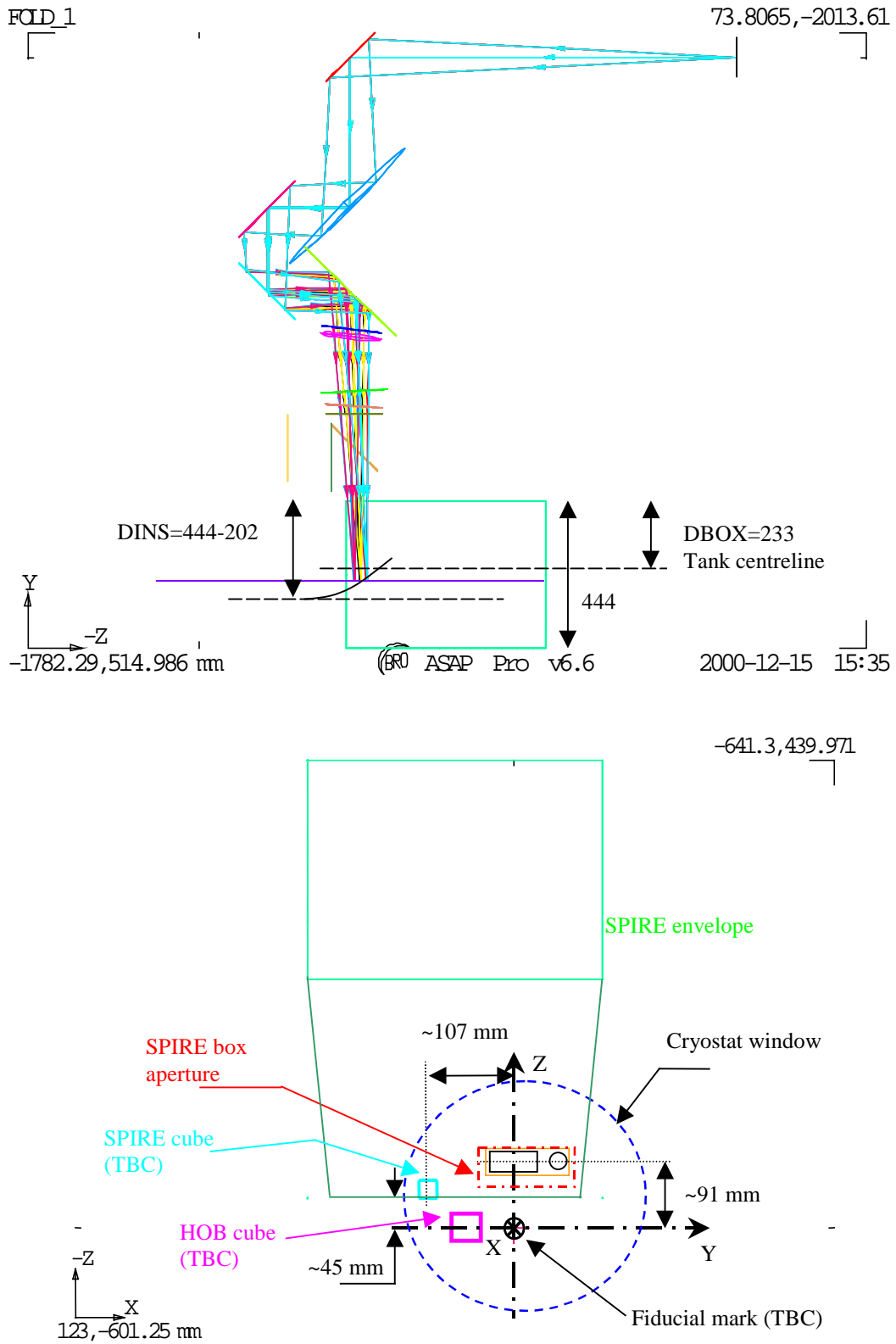


Fig.5. Spire co-ordinates system. FOV=12.55 x 4 arcmin (maximum).

The figure also shows the SPIRE alignment cube position. This shows the line of sight to the cube to be $\sim\sqrt{(107^2+[91-56]^2)} = 112.3\text{mm}$.

The global co-ordinate system used in the SPIRE optical design also has the telescope symmetry axis as one of its axes (ref.3).

The FP (parabolic surface) radius of curvature is 167.17mm (from JPL design), leading to a focus 'sag' of 24.23mm at the $\sim -91\text{mm}$ off-axis position. For the Herschel telescope Cassegrain design, the radius of curvature is 165mm, which leads to a correction of 24.55mm.

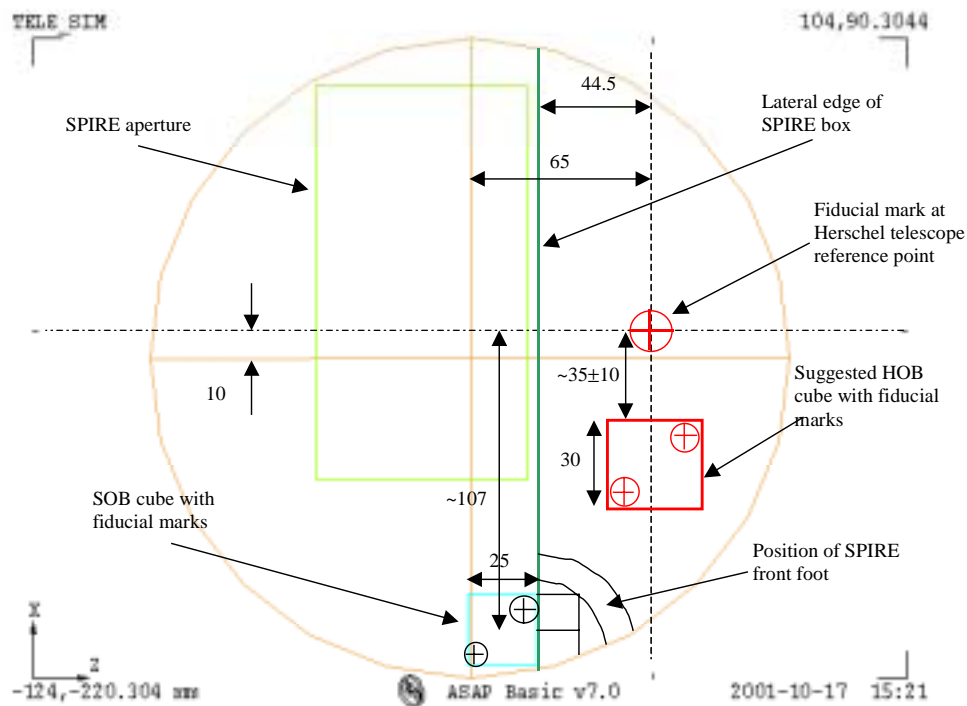


Fig.6. Details of SPIRE box aperture environment with clear aperture of visible 10K filter + filter centre (orange), with Herschel telescope focal plane axis and centre (dashed line), estimated positions ref. cubes (blue: SOB, red: HOB).

5. Cryostat internal items.

The design of filter & black body geometry are detailed in annexes 2 & 3. The latest design, which has been checked with the CAD design of the cryostat is file FIRSIM8_8.igs, shown in the figure below (it includes the correction due to the parabolic shape of the TFP surface).

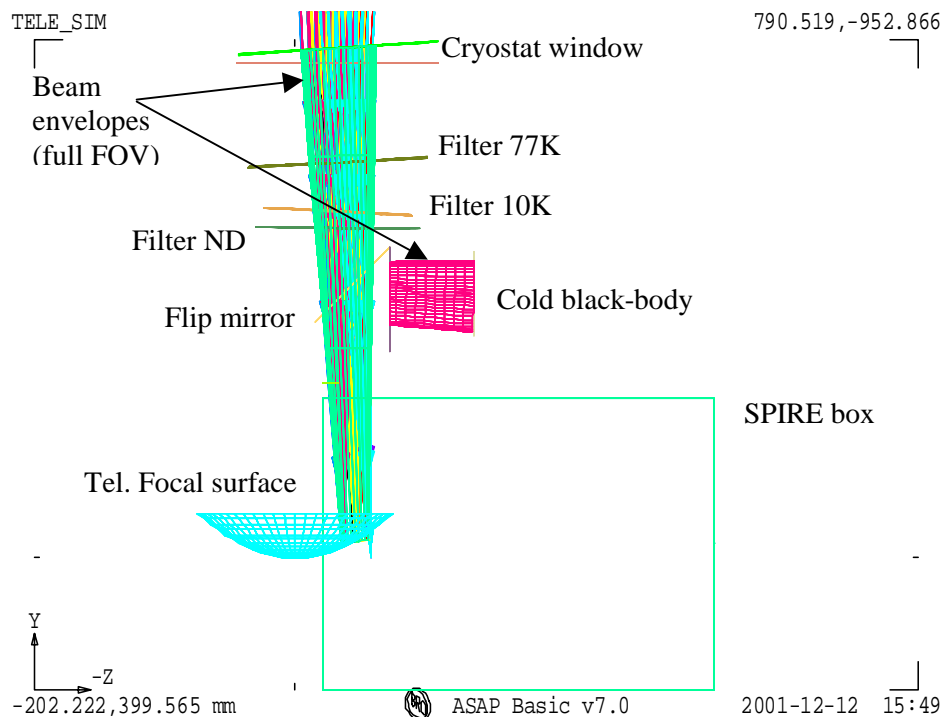


Fig.6. Cryostat internal layout for current design FIRSIM8_8.igs.

The filter positions have been set to fit the cryostat mechanical design and their tilt angles have been re-optimised for anti-ghosting (see Annex 2).

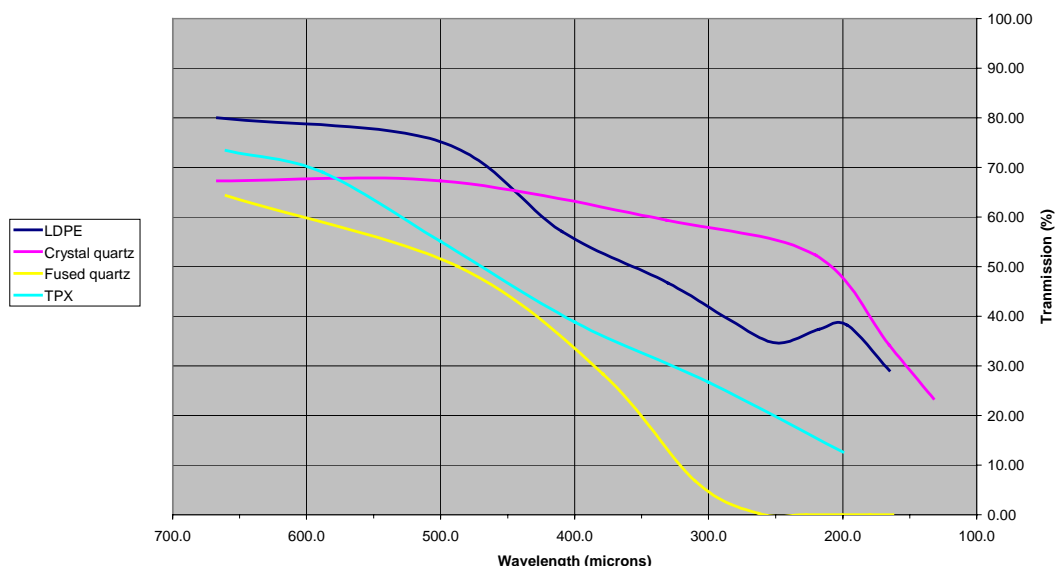
5.1. Cryostat window.

Different materials were investigated for the cryostat window. For the FIR test beam, the transmission should be the highest possible across SPIRE spectral range and for the alignment tasks (see section 8 and 9). A criterion of selection is the absorption of the FIR test beam shown in figure below for 4 different possible materials. Fused quartz, although useful because of its transparency in the visible (used for alignment check of instrument), transmits poorly in the short wavelength channel. Crystal quartz is birefringent and too costly for such a large window (~300mm diameter). Alternative polymeric materials (HDPE/LDPE, TPX) can be used. HDPE seems to represent the best trade-off but being opaque at visible, another set of window + filters are needed.

From mechanical constraint the window back surface has to be flat, so a wedge angle is needed on the front to avoid internal ghost reflections (see Annex 2) and is also used to provide the beam deflection¹ towards SPIRE input aperture. The wedge angle is a function of the material refractive index. The following filters along the optical path are also tilted with respect to the window.

¹ The incoming beam from the simulator is assumed to impinge at normal incidence on the cryostat in nominal position i.e. centre of scanned FOV.

Material transmission at FIR/sub-mm for SPIRE AIV cryostat window (~25mm thick)



A transparent fused quartz window can be used for visible check/alignment, with no extra filters (or minimal number of dummy ones i.e. replaced by thin transparent full-clear-aperture size fused quartz window). To be representative, the visible window has also a front surface wedge.

The table below summarises the results for the 2 bands with respective window material.

	Material	Refractive index (in each band resp.)	Wedge angle (window)	Filter 77K Tilt angle	Filter 10K Tilt angle	Filter ND Tilt angle
Test beam at FIR	HDPE	1.53	+3.8deg	+3.0deg	-3.0deg	-1.0deg
Alignment/Check in visible	Fused quartz	1.47	+4.3deg	N/A	N/A	N/A

The cryostat window is located at the interface with the cryostat vacuum vessel. The pressure difference would imply mechanical deformation/deflection of the window. For a FIR window in HDPE with average thickness of ~23mm, a max deflection of ~0.6mm (worst case) was estimated which transforms both flat surfaces of the window into curved ones with radius of curvature ~6-12m. The main consequence at SPIRE input plane is slight increase in spherical aberrations and defocus by <1.5mm.

5.2. Filter sizes.

The minimum clear aperture required at each filter or window surface was first calculated as shown in fig.1 below. The dimensions shown are given in the table and are used to derive the clear aperture diameter (including 20% beam oversize).

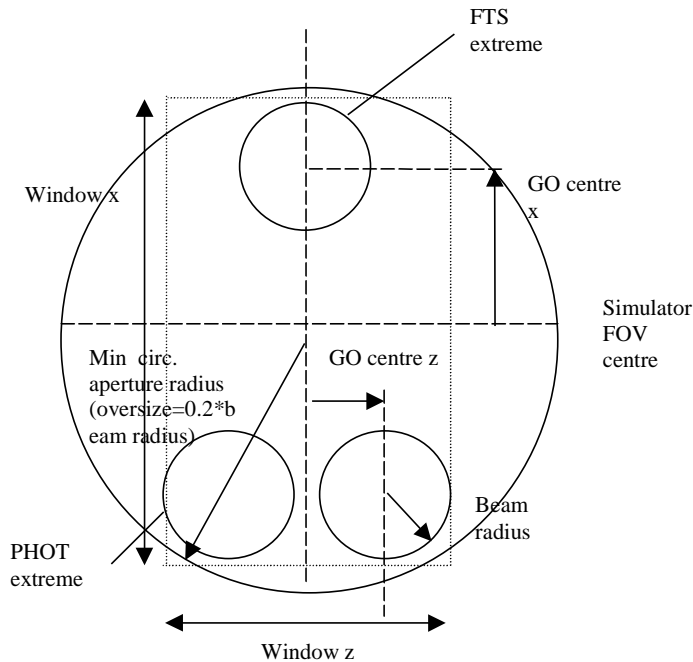


Fig.7. Geometry for calculating minimum clear circular aperture.

However fig.7 also shows that large zones of circular aperture filters that are not going to interact with main beam. Therefore a scheme to obtain the minimum rectangular filter window dimensions was derived (see fig.7 and table 1 below). Also from full FOV ray-tracing (fig. 6), a tube defining the beam envelope (including 20% oversize factor for diffraction) through the cold optical components was defined. The max linear dimensions of the “racetrack”-like beam footprints (see Annex 2) on the filters mounting surfaces are reported in table 1. Recommended values should be taken from the max. (so with a margin for eventual warm/cold variations) of these 2 latter sets of estimated values (in their respective direction). And therefore, *the resulting suggested minimal dimensions for the filters are indicated in red in the table below.*

ob GO semi-ape x	semi-ape z	separation from last surface (dist. y)	beam radius	required diameter 2R	Window x dim.	Race-track max x dim.	Window z dim.	Race-track max z dim.	surface name
52.0	N/A	0.00 (ref.)	N/A	N/A	N/A		N/A		focal surf.
47.7	N/a	N/A	N/A	N/A	N/A		N/A		box apert.
42.6	13.6	260.1	27.9	154.4	152.2	158.0	94.1	89.0	ND filter
42.1	13.5	24.9	29.4	156.9	154.7	160.0	97.5	91.0	10K filter
40.7	12.8	75.1	33.8	164.4	162.4	165.0	106.7	99.0	77K filter
37.7	12.5	151.5	42.6	179.7	177.6		127.2		window inner
37.2	12.1	22.3	43.9	181.8	179.9		129.7		window outer

Table 1: Results for *firsim8cryo_8.igs*, 12.55x4' FOV at TFP (all parameters are mm).

NB:

- It should be noted that even if all figures and plots of beam envelope take into account a 20% oversize factor for diffraction effects purpose, a possible reduction in size of the components can be expected when the system is cooled down. The thermal gradient effect needs to be compensated by further oversizing each component (depending on filters and mounting structure materials).
- The SPIRE aperture has been specifically designed separately and follows specifications from SPIRE-RAL-NOT-000694 (issue 2.01, 29/06/2001).
- The focal surface (location and size) is as per designed and specified for the ESA-Astrium HERSCHEL Telescope focal surface.

6. Simulator & sources bench layout.

The first-cut layout is shown below (Fig. 8), taking up an area of approx. 2.5 x 3.5 metres, whereas the space constraint is closer to ~1x2.5 metres. Due to this, scheme to reduce the overall simulator system size by varying R_{SM} is investigated and detailed in Annex 5.

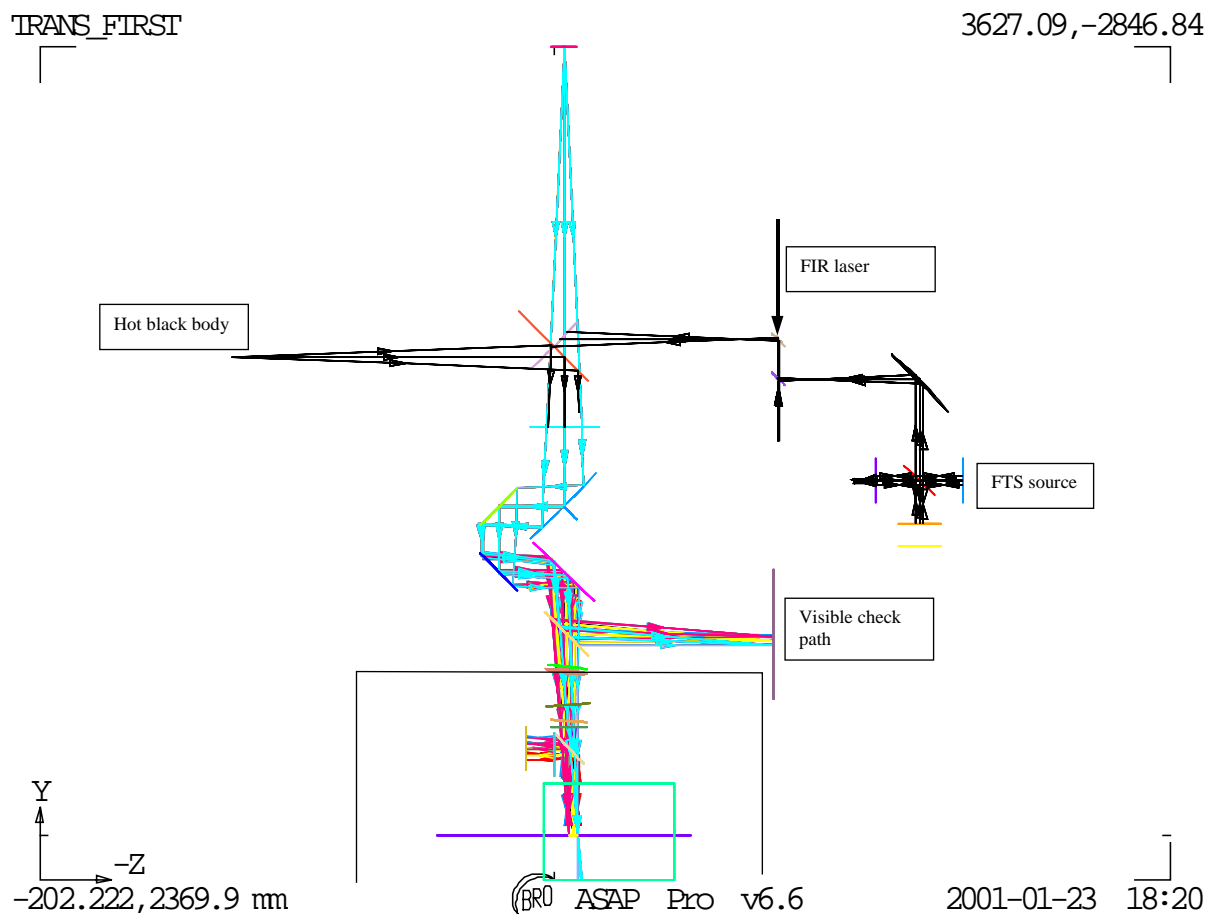


Fig.8. General system layout including sources

In addition the beam height at the cryostat is ~833mm from lab floor, and due to large size of components (imaging mirror, fold mirrors + mounting system), the optical bench may have to be no higher than ~610mm from floor, which is significantly lower than the FIR laser bench (~820 mm).

Figure 9 next page takes these heights into account as well as the space taken by the different sources (FTS, hot blackbody). For alignment purpose, a visible laser with reference pinhole R would need to be located at R_{SM} distance from the imaging mirror and in direct view - therefore F1 would be removed and the FTS system can be accommodated in place of the hot blackbody - source in order to define location of the required sources H_1 and H_2 . H_3 can be also considered as a source point for the system although realising it as one of the foci of the imaging mirror would require more measurements included in the vertical direction. Details are given in following sections. And to keep the FIR laser bench system independent, it can be considered as a provider of a collimated beam which can be injected, after re-shaping by reflective or refractive telescope (to compensate for the beam diffractive divergence over metre or more of free space propagation), into the simulator system as one of the two other points H_1 or H_2 in replacement of the other sources system.

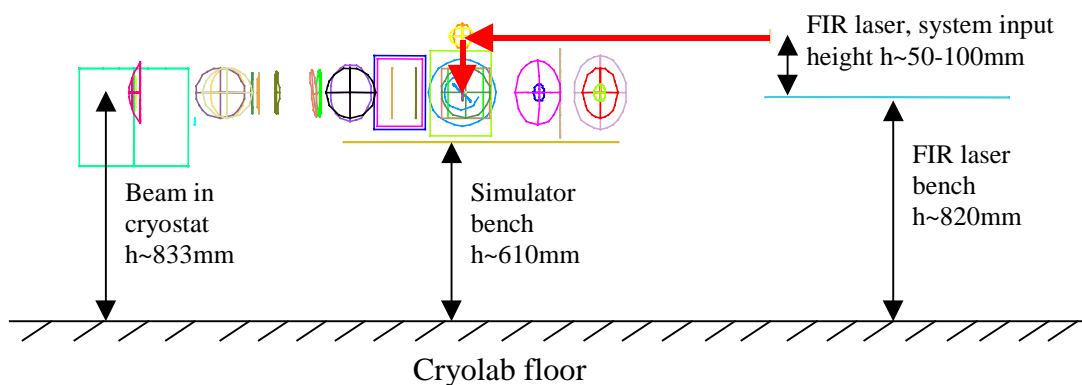
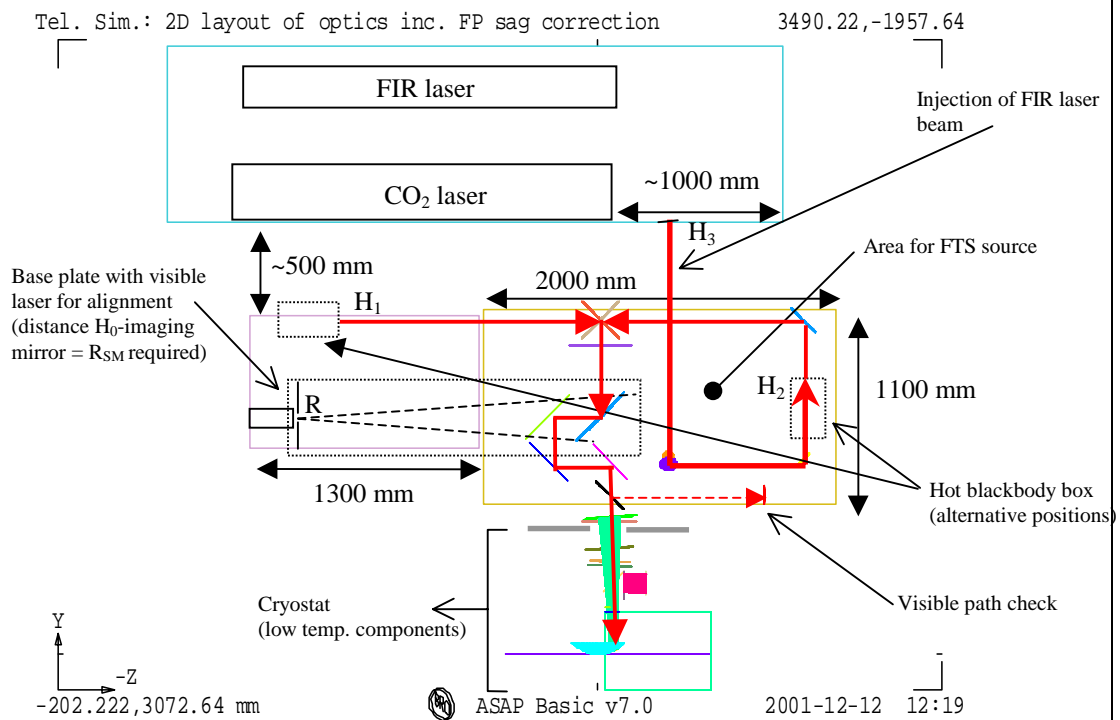


Fig. 9. *Top (Plan view)*: Layout including the FIR laser table with a possible position for a collimated beam output (system parameters: $R_{SM} \sim 1970$ mm, $DF1F2 = 250$ mm, $DF2F3 = 350$ mm with a horizontal separation set to ~ 500 mm between the 2 tables and correction, along Y, for sag. of telescope focal surface). *Bottom (Side view)*: same system; the height difference (~ 210 mm) between the 2 optical benches is better displayed in this view.

7. Pupil-scan beam mapping.

A secondary function to be performed by the telescope simulator is the scan of a point source across the pupil as another way of characterising the SPIRE instrument and also to determine the pupil actually seen from SPIRE. The preferred layout including the features required for such a scan is displayed in fig below.

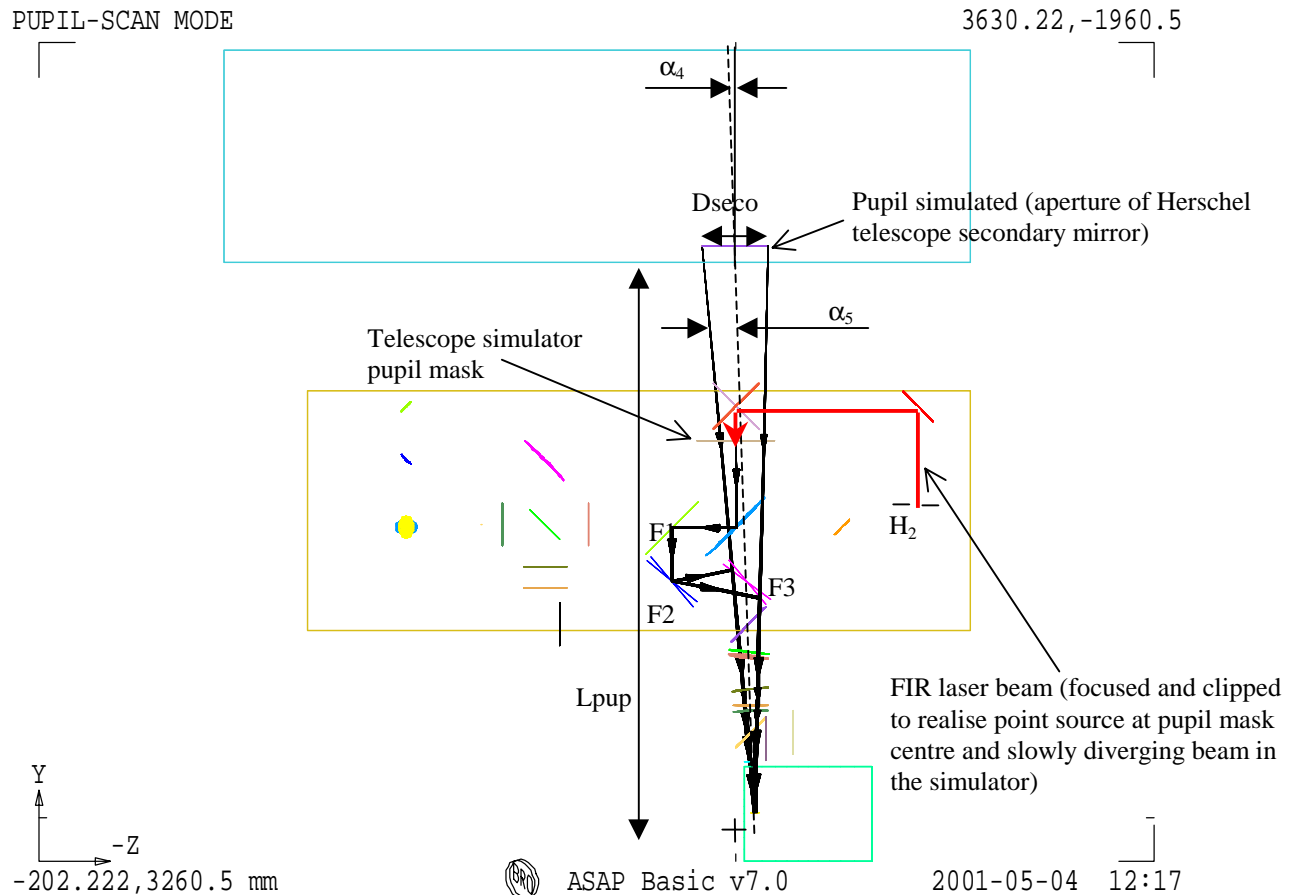


Fig.10. Telescope simulator layout (plan view). Positions for F2 & F3 are shown after required coupled rotations of both mirrors to simulate a scan across the Herschel Telescope pupil.

This scheme would not require extra actuators as F2 & F3 are already designed to be rotated about their centres and the vertical X-axis in the FOV scanning mode of the simulator. But the range in degrees (see derivation of maximum rotation angles below) would be larger than the nominal ± 4.0 deg range of the principle simulator functions (see below).

No extra translation stage is needed (contrary to what one would expect for a scan across the pupil mask). The point source is created in the centre of the pupil mask from a focused FIR laser which would have been clipped before in order to match the SPIRE field-of-view when propagating on-axis through the entire simulator (fold mirrors in nominal positions). Instrumental effects due to vignetting/clipping by limited size (constraint of space & cost) of the simulator reflective optical components would then be reduced.

- Max. range of rotation required for F2 & F3:

The beam after reflecting on F2 should be angularly displaced by θ_2 to be understood as coming from the edges of the pupil and θ_2 is given by:

$$\theta_2 = \pm \text{atan}(P_{F3}/D_{F2F3} - P_{F3}) \pm (-\alpha_5)$$

$$\text{with } P_{F3} = \tan(\alpha_{5_MAX}) \cdot D_{F3FP}$$

$$\text{and } \alpha_{5_MAX} = \text{atan}((D_{SECO}/2 - Z_{POS_SPIRE}) / (L_{PUP} - Y_{POS_SPIRE})) - \alpha_4 \sim \text{atan}((D_{SECO}/2) / L_{PUP})$$

The beam after F3 should be steered by $\theta_3 = \theta_2 \pm \alpha_5$. Finally the mirrors rotation angles are given by $\theta_2/2 \sim \pm 5.2\text{deg}$ and $\theta_3/2 \sim \pm 6.8\text{deg}$ for F2 and F3 respectively (the \pm symbol stands for the 2 extreme positions simulated at the edge of the pupil although simulating a scan beyond these limits would be useful in their determination).

The above angle ranges apply to a horizontal pupil-scan only. To include the vertical pupil scan implies a similar increase in the ranges of the vertical adjusters, and due to the 45-degree compound angles involved, these are already approx. $\sqrt{2}$ times larger than in the horizontal. Therefore the vertical case max range may be estimated as $\pm 1.4 * 6.8 = \pm 9.5$ degrees.

This required range is more than twice that of the nominal simulator functions, and the pupil scanning is seldom required (being diagnostic measurement rather than the main characterisation one). It is therefore planned that the limited range problem is overcome by making pupil scans in 2 sections for horizontal & 3 sections for vertical (i.e. not fully automated). To achieve this it is necessary to make the following steps between scan sections, i.e. whenever interrupting the scan:

1. the scan section is stopped just short of the range limit.
2. references are set up for the test beam orientation (angle & position). This is done using the verification beam path & trace visible laser.
3. The beam steering mirrors are re-jigged to the opposite end of their range, and the test beam orientation re-aligned to its references.
4. The next scan section is started.

There is an alternative scheme for pupil scanning, with the advantage of realising the actual HERSCHEL pupil (detailed in appendix). However that scheme is rejected because it requires separate & extensive scan hardware.

8. Verification of SPIRE alignment (on simulator & STM).

This function of the simulator is to meet the 4 tests required in R5-5. They must be done with the instrument cold, and so with this facility.

The tests involve checks that the alignment of SPIRE in

- 1) field position (line-of-sight),
- 2) pupil position,
- 1) remain within budget between room & operational temperatures. They do not need to include focus, as adequate focus control is ensured by the optical tolerance budget. (ref: optical error budget, LOOM.KD.SPIRE.2000.002-3).

The tests apply to changes due to:

- 2) motion of the whole SPIRE instrument (the SPIRE S-bench) relative to its mounting interface on HERSCHEL (H-bench),
- 3) motion of internal components relative to the S-bench.

The combination of these leads to 4 possible tests as per the table below. The tests can be made on the simulator & structural models and so in a separate & earlier cryogenic run to the main calibration task.

Test		Performance (Opt error budget)	Lab method	Models
Pupil,	SOB-HOB	< 6 arcmin (dr/r=3%)	Auto-collim. on SOB & HOB cubes	Verify cryo design on simulator-model. Verify SPIRE on STM
	internal	As per 'field internal'	No test.	No test.
Field (LOS)	SOB-HOB	< 0.1mm at FP	MAT telescope on SOB & HOB fiducials	Verify cryo design on HOB-model. Verify SPIRE on STM
	internal	TBD from 0.1mm, 1' per comp't	MAT telescope/PSD tool viewing D-tool	STM

A misalignment in field position places the SPIRE line-of-sight away from its nominal position within HERSCHEL field of view. This impacts the WFE performance and also the astrometric (pointing) calibration. The pointing requirement is taken here as 1% of the FOV diagonal, leading to 0.09arcmin or 0.9mm at FP surface.

A misalignment in pupil position impacts mainly the signal throughput (aperture efficiency), but also the angular response (point spread function). Since the simulator is in any case designed to characterise these aspects, the internal pupil position alignment is already tested by the nominal measurement of these parameters in the cold case, i.e. if efficiency & spatial response are in spec. then the pupil position must be OK. The (spurious) effect of changes in H-bench angle (pupil position) with cool down would not affect such a test, as this effect is taken into account in the setting up of the simulator (see section 9).

8.1 Pupil alignment.

The requirement is to show:

1. Relative angle motion of S-bench to F-bench is by less than 5.7 arcmin (4.3 mm at Herschel pupil, $\Delta R/R = 3\%$).
2. Relative position motion of instrument cold stops to S-bench is by < 3% (at instrument cold stop $3\% = \Delta R/R \sim \Delta R/20\text{mm}$, giving $\Delta R < 0.6\text{mm}$).

The **S-bench to H-bench** is to be done by means of alignment cubes mounted on the SPIRE interface plane (dummy H-bench) and on SPIRE (shown in the above figure), (S-bench). The scheme is shown in the figure below.

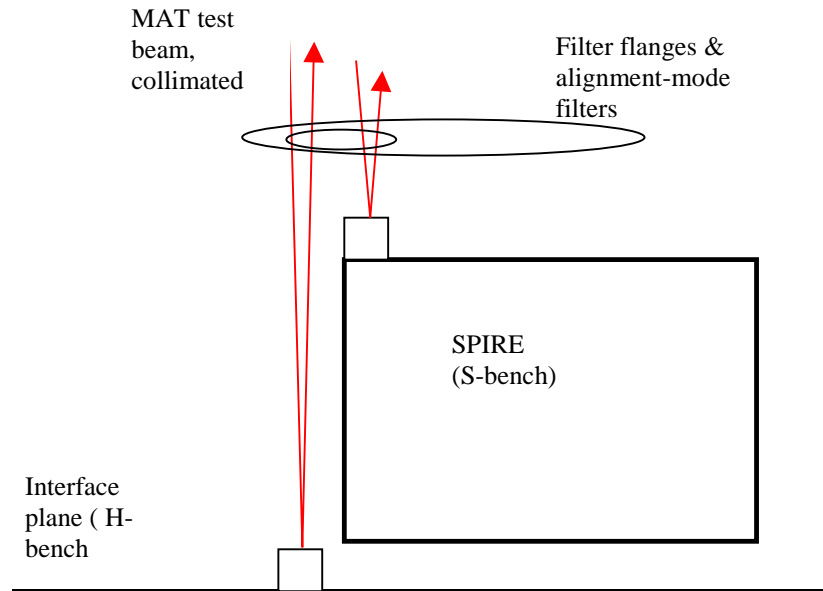


Figure 11. S-bench to H-bench angle (pupil position) check.

The relative alignment of these cubes is monitored at room T & then at cold T, to detect any changes.

The cold T requires the presence of dedicated dummy filter mounts, because the nominal filters are sized to just cover the SPIRE FOV, and do not allow access to the SPIRE cube or the interface plane. so a different set of filters will be needed for the alignment tests. The dummy mounts have clear apertures (or possibly quartz windows) , to all visible transmission, but these must be of a minimum size TBD in order to best preserve the thermal environment for this test i.e. to ensure that the added radiant heating through the apertures is not excessive.

If the H-bench cube is mounted on the baseplate as shown above, & there is a potential problem with finding its line-of-sight, as it is then deep within the cryostat, and the apertures need to be made larger than the cube size & toleranced to ensure the cube can be viewed.

The principle of the test is to locate the retro-reflections from each cube at room temperature using an autocollimator. The system is then cooled & the reflections re-located, then to determine the change in *relative* angles of the two reflections.

For the **internal angle** changes no test is required (table above), but could be done at the same time as the internal field test (next section).

8.2 Field position.

The requirement is to show that:

1. Position motion of S-bench to H-bench is by $< 0.9\text{mm}$ (impacts LOS budget, at level 1 % of FOV).

2. Position motion within instrument (defined e.g. by centre detector relative to FP referenced by fiducial mark) is < 0.09 arcmin (1% FOV).

The **S-bench to H-bench** motion of the instrument would use in the visible fiducial marks on SPIRE & the HOB cubes. Two such marks are needed per item (4 in all) to sense also rotations about the **HERSCHEL** axis, in accessible positions as shown in figure 5 earlier. To minimise the number of apertures in the filter masks the baseline is to have these marks made as etched marks on the cube coating near its corners. The limited position sighting accuracy combined with the close proximity of the marks then gives a limited accuracy in roll, TBD.

The test would be made in a similar manner to the pupil S-bench to H-bench alignment test, but in this case with the alignment telescope at finite focus (figure below). Again the test apparatus has to be scanned laterally while keeping its direction constant. This could be done using the simulator beam steering system, providing that this has sufficient accuracy. Otherwise a dedicated stable translation stage (2-axis) has to be used. Also the MAT focus has to be changed whilst be able to check that its line-of-sight is not disturbed.

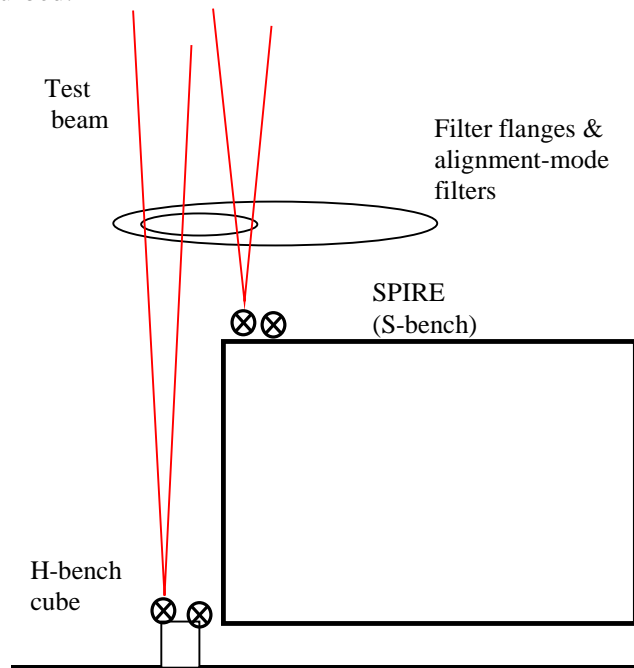


Fig.13. S-bench to H-bench position (= line-of-sight) test.

For the **internal** position motion test, the SPIRE D-tool would be used, as shown in the figure below.

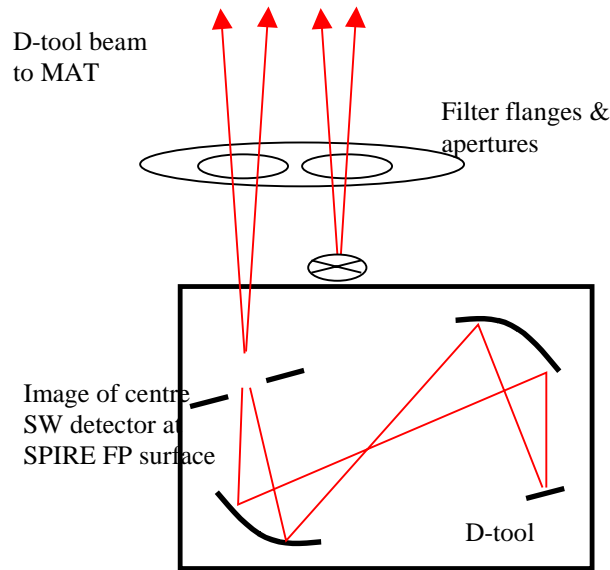


Fig.14. Internal position (= line-of-sight) alignment test.

The principal of the test is the same as the previous one, except that here the D-tool can provide the illumination rather than the MAT itself. In the warm test a position sensitive detector (PSD) is used at the SPIRE FP surface. In the cryostat test the D-tool LED's have IR emission & can only be used with the PSD, not with visual alignment as per fig.14. It is desirable that the D-tool can be referenced directly to the SPIRE fiducial marks, in order to include all possible contributions to field misalignment, and for this purpose a visible source is required on the D-tool, and is incorporated in the tool as fibre-coupled light. In order to sense detector rotation about line-of-sight it is necessary to view corner(s) of the FOV (detector array) as well as the centre. To avoid using too large an aperture in the filter masks just 2 FOV positions will be used. The test then requires a max. of 4 apertures in the dummy filter mount (2 SPIRE pixels + 2 fiducial marks).

By adding a dummy FP mask in this test we could distinguish between changes within the optics and in the optics/box/cube.

Ideally all of these alignment verification test would be done in the same cryogenic run. This requires up to 4 apertures in the dummy filter plate, made up of: 2 detector (FOV) pixels, 1 prism on SPIRE including 2 fiducial marks, and 1 prism on the H-bench also including 2 such marks.

For a reduced scheme, on the simulator model only the external alignments are checked, requiring only 2 apertures (SPIRE & HOB cubes). If these tests don't need to be repeated on the STM model, then that test would be just internal & so not need the HOB cube, leading to 3 apertures.

9. Setting up the simulator.

The alignment of simulator optics has to ensure that (figure 15):

1. Reference pinhole apertures 'H' are positioned sufficiently close to the imaging mirror input focus such that when the sources are sent through them they are imaged with low aberration (WFE).
2. The source+mirror system is correctly positioned with respect to the **cold** instrument such that the mirror output beam is aligned in :

- (a) Linear position: Focus 'S', at the nominally centred beam steering position, sufficiently close to the SPIRE FOV centre at the input FP surface (this is needed to ensure that the range of beam steering & focus is sufficient to cover the required range);
- (b) Angular position: Simulator exit pupil position sufficiently close to instrument entrance pupil location laterally in $\Delta R/R$ terms for the simulator beam to be representative of the HERSCHEL beam.

To meet the requirement (1) within the above-restricted available space, an alignment procedure has been devised which uses a reverse-direction laser trace beam through a reference pinhole R (at mirror focus), as per the figure below. R is permanently set relative to the mirror centre O, and the laser sent through R & O back towards the source references H. In this way the correct source positions can always be referenced correctly & quickly, regardless of how much folding is needed in the input paths & how often it is required to switch between sources.

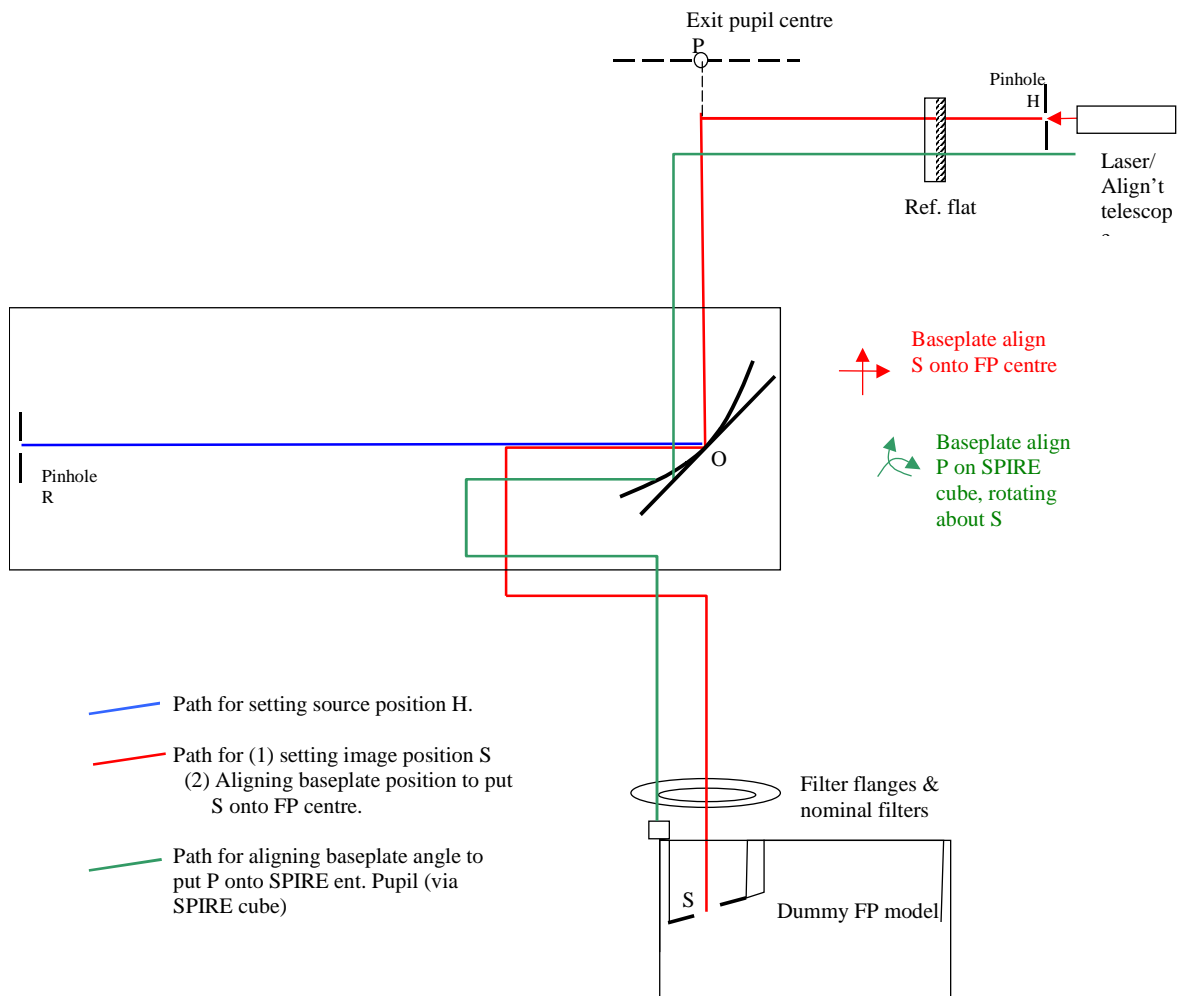


Figure 15. Scheme for realising permanent point-source reference position R.

To meet requirement (2a), (relative positioning of simulator to cold SPIRE), the only option is to make a best nominal position of the simulator before cooling the STM or QM. This should be done using a dummy FP surface with fiducial marks, viewed via the simulator (as per the LWS scheme). As long as the motion on cooling is within the SPIRE fov angle range (± 1.5 times 3 cm at the FP, plus similar

amount of scan-able range), the aiming of the simulator beam signal should be successful in hitting e.g. the p/SW array. The FOV position error can then be measured in 2 axes. The simulator focus adjustment can then be exercised to determine the simulator's focus error (simulator position error in the 3rd axis). The data so derived can then be used to move the simulator (moving O & R together on same baseplate, followed by re-positioning of H), before re-checking. In this way the simulator in its centre-range state is centred up on SPIRE using the QM, and ideally neither cryostat nor simulator mirror focus r are then moved until arrival of the flight model.

For the requirement (2b), simulator pupil position tests similar to the previous instrument alignment tests could be used. I.e. either the SPIRE alignment cube is used to reference the pupil direction, or the pupil scan is used to realise the whole SPIRE entrance pupil. The former option is preferred for simplicity, but requires that a flat mirror be used in place of the simulator mirror at point O (green ray path in figure 15). The procedure for sighting the SPIRE cube is then:

1. Replace simulator mirror with large flat, align this such that incident laser spot location, and reflected laser beam direction are preserved.
2. Introduce reference flat mirror at laser source. Use this to laterally translate laser to the (expected) location of the SPIRE cube.

Admitting this laser beam to the system will then locate the SPIRE cube and the direction of the return beam indicates the angle orientation (pupil lateral misalignment) of the simulator to the instrument.

This test locates the instrument pupil relative to the simulator axis. Having measured or derived the pupil offset at the M2 location it is to be corrected by again moving the whole simulator. To respect the results of the test for (2a), the motion would be a rotation about the output focus position, and detailed metrology plus calculation will be required to manoeuvre the simulator into position on the QM with respect to both requirements (2a & 2b) simultaneously. It is therefore required that (2a & 2b) be testable simultaneously.

10 Sources.

The point-like sources are required to be fed through the simulator in its nominal PSF-measuring scanning mode are detailed in the requirements document ref.9. For purposes of the design description they can be summarised as:

FIR laser. Mostly coherent source i.e. clearly defined near gaussian beam shape, monochromatic.

Hot BB. Incoherent source but with pinhole aperture which can be varied to select different degrees of spatial coherence & hence beam-shape (within limits). Broadband.

FTS source. Source as per Hot Black body, but pinhole aperture being the FTS field stop. The selection of this must respect the spectral resolution constraints.

All of these are regarded as point-sources for the purpose of the imaging mirror design, although there are small long-wavelength beam errors due to the simple form of the imager.

In addition a source is needed for generation of the pupil-scan, and the FIR laser is selected as the best source for this purpose because with appropriate mask its aperture size (f-number) and position can be most precisely defined.

In addition there is a requirement for '**extended sources**' to be presented to the instrument via the simulator. Ideally this would be a uniform source, which instantaneously fills the whole SPIRE field-of-view. Although such a source could be realised, e.g. using a hot BB of size equal to SPIRE's FP

aperture (~ 6 x 3 cm for PHOT), it would not be correctly imaged through the simulator, because the imaging mirror is defined for a point-source only i.e. except at the on-axis point there would be no one-to-one correspondence between source and image points, nor would the pupil be correctly realised. This would mean that in for example a field-flatness test, the resulting detector signals would have a more uniform spread of values than would be the case for a correct extended field arrangement. Extended sources of smaller size (a few pixels) might be used, although these would still have significant imaging aberration & pupil error.

Annex 1. Telescope simulator control laws.

CONTENTS.

1. Zero-offset case.

1.1. Control of beam for fov.

Horizontal, (In plane of diagram).

Vertical.

1.2 Focus control.

a. Centre of SPIRE fov.

b. Defocus with FOV.

Horizontal

Vertical.

2. Case with offset mirrors.

2.1 Horizontal FOV.

Ray at F2

Approx. solution for ray at F2

Ray at F3

Approx. solution for ray at F3

Vertical FOV

3. Laws modelled with Zemax

3.1 Elements Included

3.2 Exclusions

3.3 Future improvements.

1. Zero-offset case.

The figure below is to show the parameters used to set up the ray-trace model above.

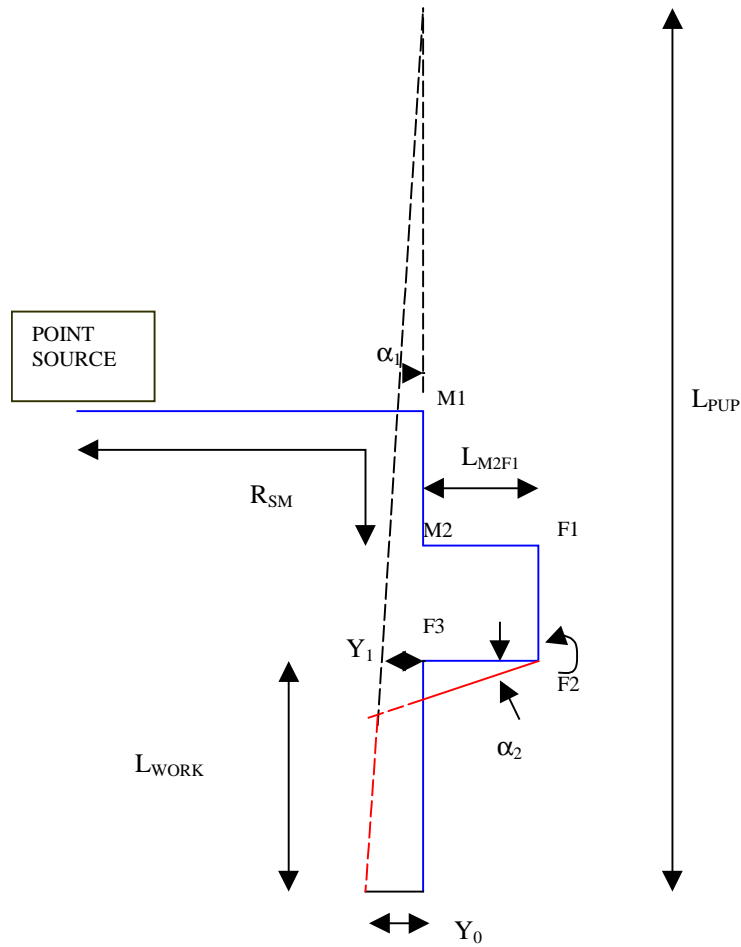


Fig. Parameterised layout of to show the control-laws.

In the figure the path of the optic axis is shown in blue for centre of SPIRE fov & in red for the edge.

1.1. Control of beam for fov.

Horizontal, -In plane of diagram.

The steering in angle & position are made by combined ‘walking’ of F2 & F3 to generate the correct output pupil.

To first order (I.e. for small fov angle α_1):

$$Y_0 = \text{fov_rad} * F_{\text{TEL}}$$

$$\alpha_1 = Y_0 / L_{\text{PUP}}$$

where fov_rad is the required field of view radius position (telescope object space), F_{TEL} is the telescope focal length (28.5m), L_{PUP} is the secondary mirror to SPIRE input focal point.

Dimension Y_1 is given by

$$Y_1 = \alpha_1 \cdot (L_{\text{PUP}} - L_{\text{WORK}})$$

And

$$\alpha_2 = Y_1 / L_{\text{F2F3}}$$

$$\alpha_3 = \alpha_2 - \alpha_1$$

in the small-angle approximation, where L_{F2F3} is the distance from mirror F2 to mirror F3.

In the figure, $L_{\text{F2F3}} = 250\text{mm}$, the same for the other fold mirror separations, adequate for handling the beam size at 45 degree incidence.

$$L_{\text{WORK}} = R_{\text{SM}} - (L_{\text{M2F1}} + L_{\text{F1F2}} + L_{\text{F2F3}})$$

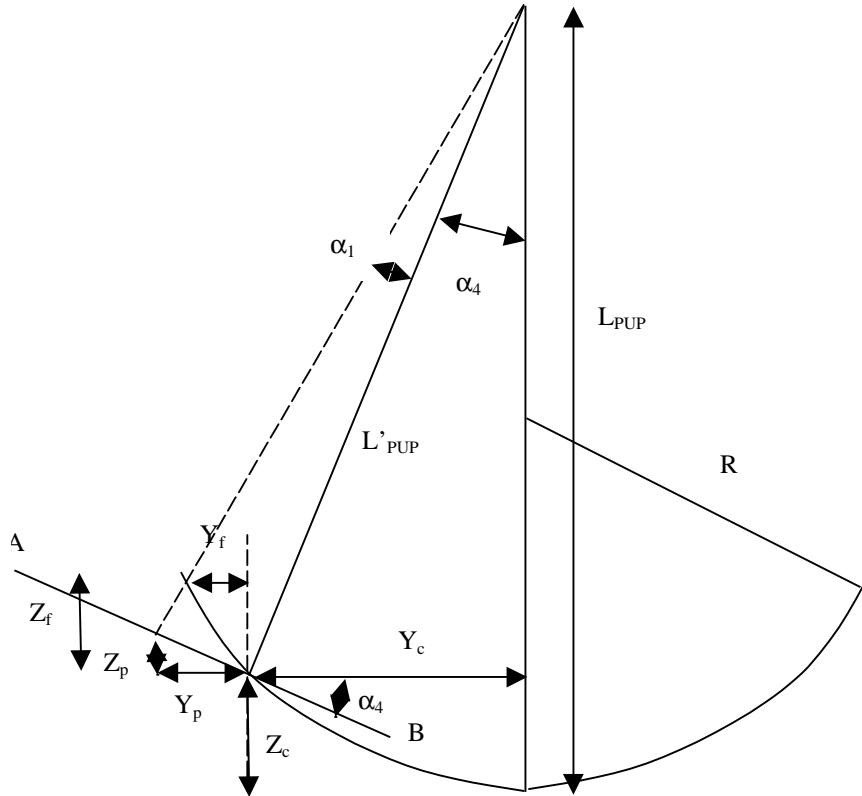
For the horizontal FOV, the 2nd fold mirror F2 is moved anti-clockwise through angle $\alpha_2 / 2$, and the 3rd mirror F3 also anti-clockwise, by $\alpha_3 / 2$.

Vertical.

To generate the FOV in the other axis, i.e. that perpendicular to the plane of the diagram (X-axis), to 1st order the same angles α_2 α_3 are used, but are for this case rotations about the Y-axis. The magnitudes of the mirror rotations are larger by a factor of $\sqrt{2}$, since the mirrors are tilted at 45 degrees to the angle of incidence. This is accurate when steering in the vertical only, and is correct to first order for the FOV to be simulated i.e. with combinations of horizontal and vertical steering.

1.2 Focus control.

The correct, non-planer focal surface for SPIRE (not shown in ray-trace fig.1.) would be generated by additionally translating fold_1 & fold_2 on the 'trombone' arrangement.



Equation of focal surface:

a. Centre of SPIRE fov.

Denote this position (X_c, Y_c, Z_c)

$$Z_c = R \cdot (1 - \sqrt{1 - (Y_c/R)^2}) \text{ for a spherical surface approximation}$$

$$\text{or } Z_c = Y_c^2 / 2R \text{ for the parabolic focal surface}$$

$$Y_c = \sin \alpha_4 \cdot (L'_{PUP}) \text{ (NB changed from last version)}$$

α_4 is SPIRE's off-axis position, given by

$$\tan \alpha_4 = \text{fov_pos} \cdot (F_{TEL} / L_{PUP})$$

where $\text{fov_pos} = 11 \text{ arcmins}$.

The equations for Y_c, Z_c are solved simultaneously to give the centre position (Y_c, Z_c) .

L'_{pup} is given by

$$L'_{pup} = Y_c / \sin \alpha_4$$

b. Defocus with field angle.

Horizontal (Y).

At fov angle α_1 (as per fig.2) , the co-ords are:

For plane AB:

$$\tan.\alpha_1 = \Delta/L'_{PUP}$$

Where Δl is the distance along AB, given by (positions on plane denoted by subscript p):

$$\cos.\alpha_4 = Y_p/\Delta l$$

Together this gives:

$$Y_p = L'_{PUP} \cdot \cos.\alpha_4 \cdot \tan.\alpha_1$$

Z on the plane can be found from

$$Z_p = \tan.\alpha_4 \cdot Y_p$$

FP surface Sphere/parabola.

Positions on this surface denoted by sub-script 'f'.

$$Z_f + Z_c = R \cdot (1 - \sqrt{1 - ((Y_c + Y_f)/R)^2})$$

$$\text{or } Z_f + Z_c = (Y_c + Y_f)^2 / 2R \text{ for paraboloid}$$

$$Y_f + Y_c = \tan.\{\alpha_4 + \alpha_1\} \cdot [L'_{PUP} - (Z_f + Z_c)]$$

Solve the above two equations for Y_f , Z_f . In the paraboloid case, substituting the Z equation into the Y equation gives a quadratic in $(Y_f + Y_c)$, and so is easily solved. The +ve root is required in the quadratic solve.

The focal correction required to be applied is $-\sqrt{[(Y_p - Y_f)^2 + (Z_p - Z_f)^2]}$

In addition, there is already a focal curvature of radius L'_{PUP} , i.e. by sag amount

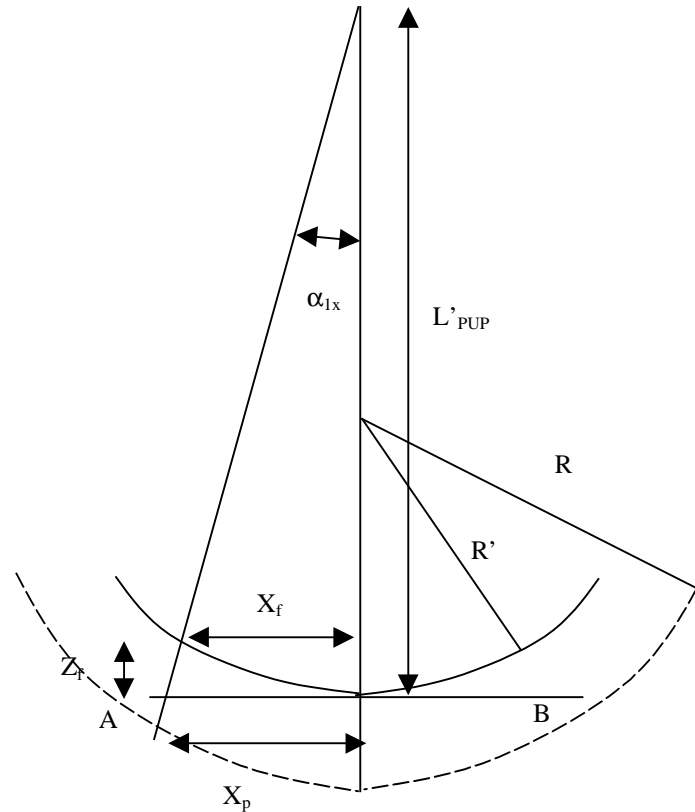
$$\sim -\Delta l^2 / (2 \cdot L'_{PUP})$$

To reach the correct focal surface, the F1 + F2 trombone arrangement should be moved to the *right in the figures* by $\frac{1}{2}$ of the difference, i.e. a total distance:

$$\Delta Z(\alpha_{1y}) = [\sqrt{[(Y_p - Y_f)^2 + (Z_p - Z_f)^2]} - \Delta l^2 / (2 \cdot L'_{PUP})] / 2$$

again this is correct only for small-angle changes, i.e. those which give small total variation in path lengths around the 45-degree mirror arrangement. Also the square root may be +ve or -ve.

Vertical (X).



The diagram is in a plane perpendicular to that of the horizontal case, and parallel to the line of L'_{pup} .

Again from along a line AB we take a plane:

$$\tan.\alpha_{1x} = X_p/L'_{pup}$$

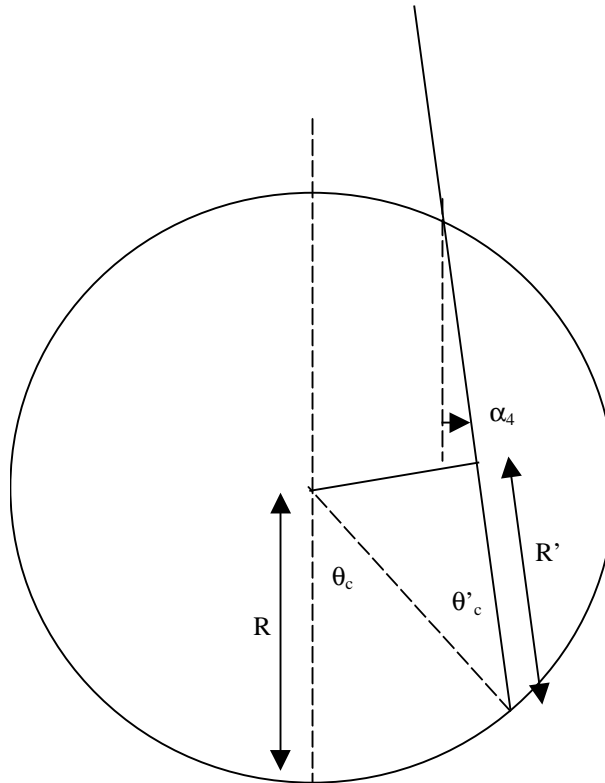
And a focal surface:

$$\begin{aligned} Z_f &= R' \cdot (1 - \sqrt{1 - (X_f/R')^2}) && \text{- sphere} \\ Z_f &= X_f^2/2 \cdot R' && \text{- paraboloid} \end{aligned}$$

$$\tan.\alpha_{1x} = X_f/(L'_{pup} - Z_f)$$

For the parabola case used the 2 equations can be combined, e.g. to make a quadratic in X_f for solving.

The parameter R' has to be determined, and for the case where FP is a sphere it is the radius of a latitude line (non great circle) on the sphere of radius R , due to its intersection with the plane of vertical scanning (formed by L'_{pup} and X , i.e. the plane of the above diagram). The geometry of the non-great circle is shown below.



From this we have

$$\begin{aligned} R' &= \cos.\theta'_c.R \\ &= \cos(\theta_c - \alpha_4).R \end{aligned}$$

The defocus to apply is then as before, but with $\Delta l = X_f$ (NB: in the horizontal case $X_f \sim X_p$ was effectively taken).

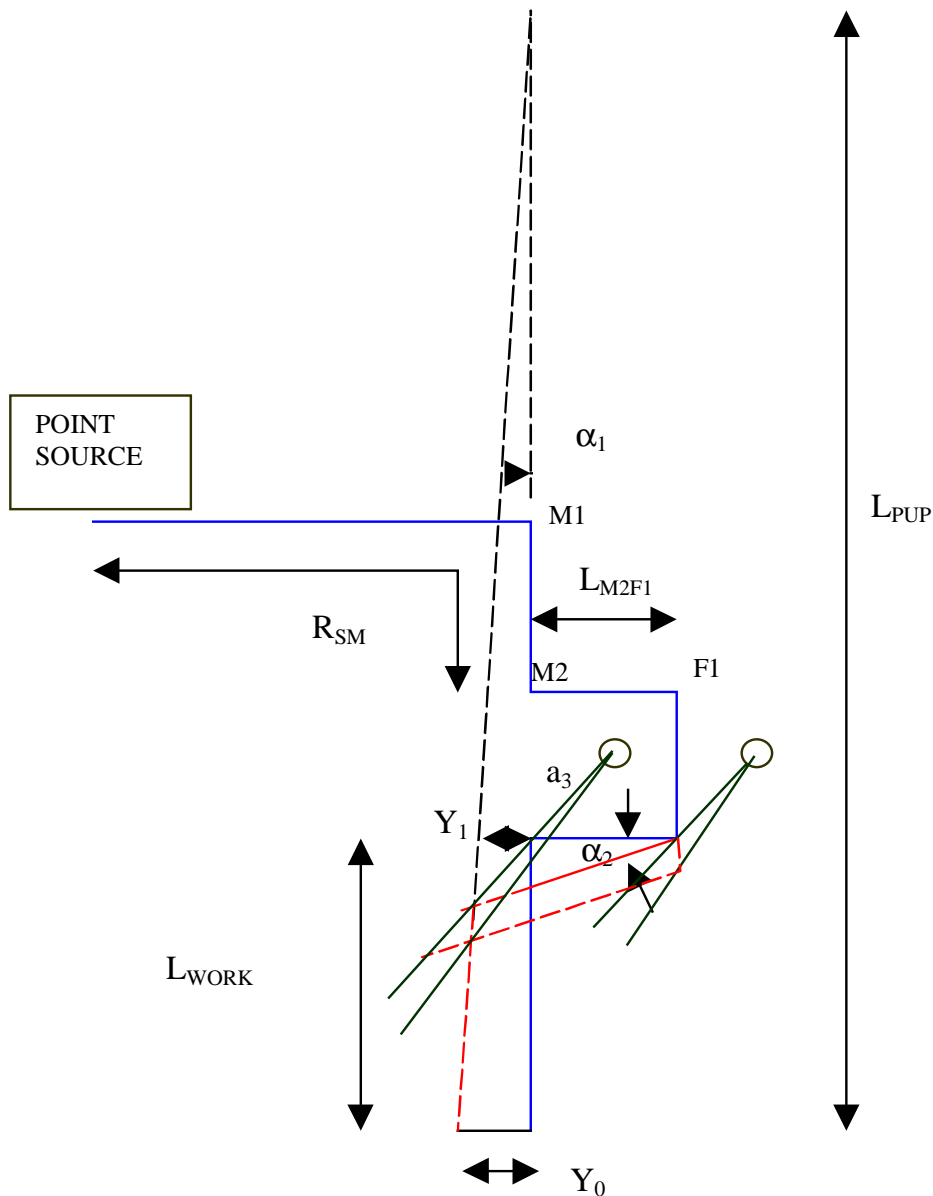
$$\Delta Z(\alpha_{1x}) = [\sqrt{[(X_f - X_p)^2 + (Z_f)^2]} - X_f^2 / (2.L'_{PUP})] / 2$$

In this case the square root is always positive because $R' < L'_{pup}$.

To combine the defocus due to each axis, a root sum squares should be used.

2. Case with offset mirrors.

2.1 Horizontal FOV.



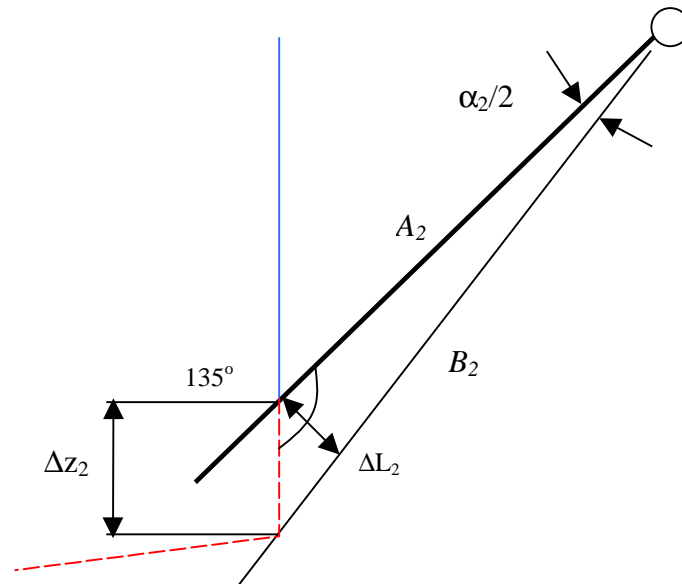
Above figure: Parameterised layout to show the offset control-laws. In both horizontal & vertical cases the offsets should be arranged to be in the same global direction, for optimum compensation of the effect between mirrors.

In the figure the path of the optic axis is shown in blue for centre of SPIRE fov & in red for the edge, i.e. as per fig.1.

The steering in angle & position are made by combined 'walking' of F2 & F3 to generate the correct output pupil. The following section deals with the case of lateral mirror offsets, where the centre of rotation is shifted along the surface of the mirror. The case of 'thickness' offsets is discussed later.

Ray at F2 mirror.

The rotation point being offset by distance 'a' from the axis causes the impact point on F2 to also drop by a distance Δz as shown below.



delta-z is given by

$$\frac{\sin(\alpha_2 / 2)}{\Delta z_2} = \frac{\sin 135}{b}$$

The 3rd side length b must be found from the triangle law

$$b^2 = a^2 + \Delta z_2^2 - 2.a.\Delta z_2.\cos 135$$

combining these last two equations gives a quadratic for $\Delta z(\alpha)$:

$$\Delta z^2 \left(\frac{\sin^2 135}{\sin^2 \frac{\alpha}{2}} - 1 \right) + \Delta z.(2.a.\cos 135) - a^2 = 0$$

A similar shift occurs at the F3 mirror, and for the rotation points as shown above, it has the effect of compensating for that at F2.

- Approximate Solution at F2

The distance ΔL_2 can, for small angles, be approximated to:

$$\Delta L_2 \approx a_2 \cdot \frac{\alpha_2}{2}$$

where ΔL_2 is perpendicular to the nominal mirror surface.

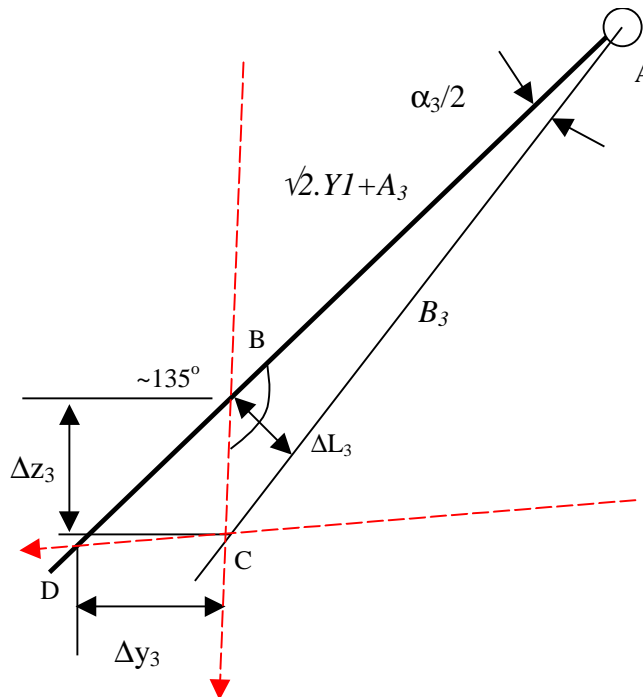
Now, Δz_2 is the long side of a triangle, and is given by:

$$\Delta z_2 \approx \sqrt{2} \cdot \Delta L_2$$

This eliminates the need to solve the quadratic equation, using a 'feed-forward' method, as per the control laws without offsets.

The alternative solution continues after the F3 mirror is considered.

Ray at F3 mirror.



In this case a must be replaced by $a + (\sqrt{2}) \cdot Y1$. a_3 is the offset, in the nominal position. B_3 and Δz_3 are found from the triangle ABC.

Δy_3 is found from Δz_3 using the triangle BCD, for which angle $b = 45 - \alpha_1$, and angle $c = 90 + \alpha_2$.

In the face of these shifts, we wish to maintain the final position Y1 on the 3rd mirror, so we have approximately.

$$Y1 = L_{F2F3} \cdot \alpha_2 + \Delta z_2(\alpha_2) - \Delta y_3(\alpha_3, Y1)$$

From which to find the correct α_2 and α_3 as before.

The previous relation

$$\alpha_3 = \alpha_2 - \alpha_1$$

still holds, so that in the equation for Y1 the only unknown is α_2 .

Therefore for a given requested field position (Y_0), and known mirror offsets a_2 and a_3 , an implicit equation is to be solved for α_2 . This is approximate in '1st order' as per the previous laws.

- Approximate Solution at F3 and Overall

Using a_3' as defined above, ΔL_3 is given by:

$$\Delta L_3 \approx a_3' \cdot \frac{\alpha_3}{2}$$

As before, this can be used to find Δy_3 :

$$\Delta y_3 \approx \sqrt{2} \cdot \Delta L_3$$

Hence Y_1 is defined explicitly as:

$$Y_1 = L_{F_2F_3} \cdot \alpha_2 + \Delta y_2 + \Delta y_3$$

At this stage, the angles α_2 and α_3 are both used to define Y_1 . Y_1 itself is related to the field angle α_1 , by the same equation as in the control laws without offsets.

$$Y_1 = \alpha_1 \cdot (L_{pup} - L_{work})$$

The system of equations is closed by using:

$$\alpha_3 = \alpha_2 - \alpha_1$$

allowing the mirror angles to be found one at a time.

The final equation for $\alpha_2/2$ has the following form:

$$\frac{\alpha_2}{2} = \frac{Y_1 - \sqrt{2} \cdot a_3' \cdot \alpha_1 / 2}{2L_{F_2F_3} + \sqrt{2} \cdot (a_2 - a_3')}$$

This is similar to the equation for the control laws without offsets:

$$\frac{\alpha_2}{2} = \frac{Y_1}{2L_{F_2F_3}}$$

but with offset-dependent corrections.

2.2 Vertical FOV

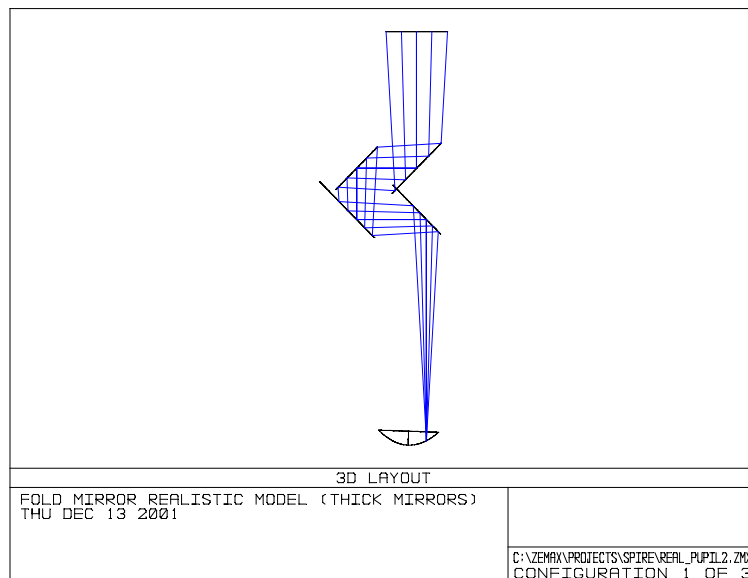
The mirror rotations are then calculated in the same way as for the control laws without offsets. Although it is not immediately clear how, the above scheme is applicable in the vertical plane as well. Care must be taken when defining the direction of the mirror offsets, in order to achieve the correct

results. In all cases above, the values of ‘a’, the lateral offsets, are taken as positive. A multiplication factor of $\sqrt{2}$ is again used to calculate the vertical mirror rotations needed for a given α_2 and α_3 .

Note that this scheme deals exclusively with lateral offsets in mirror rotations. The so-called ‘thickness offset’, caused by the mirror-mounts rotating about a point behind the surface of the mirror, is ignored in this scheme. The impact of this is can be approximated, by testing the above control laws for a system with and without thickness offsets. The performance is found to be very similar in each case, so it is safe to ignore them in the control laws.

3 Laws Modelled with Zemax

A Zemax ray-trace model has been used to implement these control laws. The model is real, as it includes all the physical factors of the laboratory set-up intended to be used for the simulator. The principle is that, whatever control laws are used to generate the FOV, it should be possible to model the outcome. Therefore, the model includes all the dimensions, offsets, rotations and translations that will be implemented (some of which have been practically tested) in the lab. See figure below.



Zemax model, plan view of lab arrangement (*NB*: the direction of trombone is reversed, see the previous schematic diagrams).

3.1 Elements Included

The model is based upon the nominal state of the telescope simulator, as shown by the blue ray in the first diagram. At this point, the virtual pupil is that seen by SPIRE in the central pixel of the photometer arrays. The Herschel focal surface is included, and the model is precisely built to give best focus when the mirrors are not tilted from their nominal orientation. Also included is the capability of translating the F1 and F2 mirrors together, to simulate the focal corrections given by the focus control law. By tracing the gut ray through the system, the path lengths between each component surface can be found, and used as a reference for simulated steering manoeuvres.

The mirrors F2 and F3 may be tilted, by selecting values of horizontal and vertical rotation with respect to the nominal position. This is done in the order: horizontal first, then vertical. This has a physical significance within the ray-trace model, but may not be an issue for the real mirror mounts in the experiment. The mirrors themselves are defined so as to rotate about a point, which is offset from the nominal beam intercept in all three dimensions. The magnitudes of the offsets can be varied within the model, to match a particular lab configuration.

Using macros designed to implement a scan sequence (a set of different mirror angles and focus positions), the performance of the control laws may be tested. The control laws actually give the beam deflections required (α_2 and α_3) for a particular FOV position. They must first be converted into mirror rotations, as described (by equation for α_2 and α_3) at the end of section 1.1. The macros provide for calculation of the offset control laws, and the full focus correction scheme described in section 1.2. The offsets and other dimensions are first read from the Zemax model, and processed to match the sign conventions for the control laws. The resulting mirror rotations are then loaded into the Zemax model, to allow ray-trace tests to be carried-out on each FOV position. The macros also allow tests to be done both before and after the focus correction is added. Included are checks to ensure that the correct signs are used within the focus control law calculation (see section 1.2). The resulting scan data is written out to a text file, which may then be read-in to a spreadsheet for analysis.

3.2 Exclusions

The control laws do not account for all aspects of the simulator's complex behaviour. All the control laws implemented are 'first-order' approximations. The following additional assumptions have been made:

1. The horizontal and vertical axes are separable. Compound angle effects will appear whenever steering is made in both axes. This has the effect of producing rays at slightly different angles to those that were input. Consequently, the focus calculations will be performed for the wrong FOV angles, and so will include some inaccuracy beyond their first-order nature.
2. Another effect of importance is that the focus correction applied causes the beam intercept at the F3 mirror to change slightly. This is not taken into account by the control laws, meaning that an additional error will appear in the resulting focus.
3. Further, the path length expected by the focus control laws is that in the nominal steering position. This changes slightly across the FOV, and is made worse by the mirror offsets.
4. The focus control laws also assume perfect pupil position simulation during steering (no pupil error $\Delta R/R$). The $\Delta l^2/2 L'_{\text{pup}}$ part of the control law is therefore not quite correct.
5. In the vertical focus control law, no attempt has been made to compensate for the horizontal steering. The radius of curvature of the focal plane is assumed to be that at the SPIRE off-axis location (R'). This is equivalent to using $\sqrt{2}$ to find the vertical mirror rotation for all horizontal steering angles.

3.3 Future Improvements

Two corrections to the control law scheme are already possible.

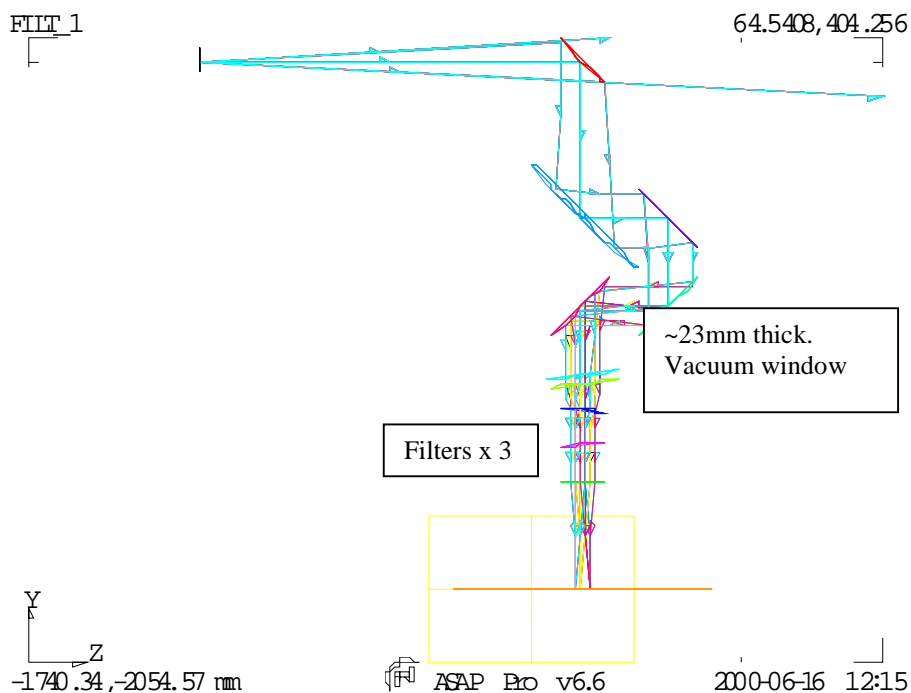
First, the approximations in mirror rotations may be made exact, hence giving the expected final beam angle α_1 . This is possible by considering 3-D vector geometry at F2 and F3. A solution for this has been formulated, and can be initiated if so desired. While this may not give smaller pupil errors (which depend on how good the control laws are), it may reduce the focus errors, as well as improve 'pointing accuracy' (where the beam ends up on the input focal plane).

Secondly, the reliance on the focus control law approximations can be addressed. An interesting aspect of the Zemax model is that, despite all these exceptions in the control laws, the results are still predictable. This leaves open the possibility of using ray tracing to find the necessary focal correction for a given FOV position. The current analysis macros are capable of this, but only to first order. It may be the case that with so many exceptions, focus will only be sufficiently controlled using this method. Since the focus tolerance has not been confirmed (<1mm TBC), no definite conclusion can be reached. It is also likely that the focus performance will vary with the magnitude of the mirror offsets.

As the design comes closer to being finalised, it should be possible to reach a decision with the existing software, and to take any necessary action as a result. This would however represent a more significant departure from the model philosophy, by relying on ray-trace calculations rather than explicit solutions.

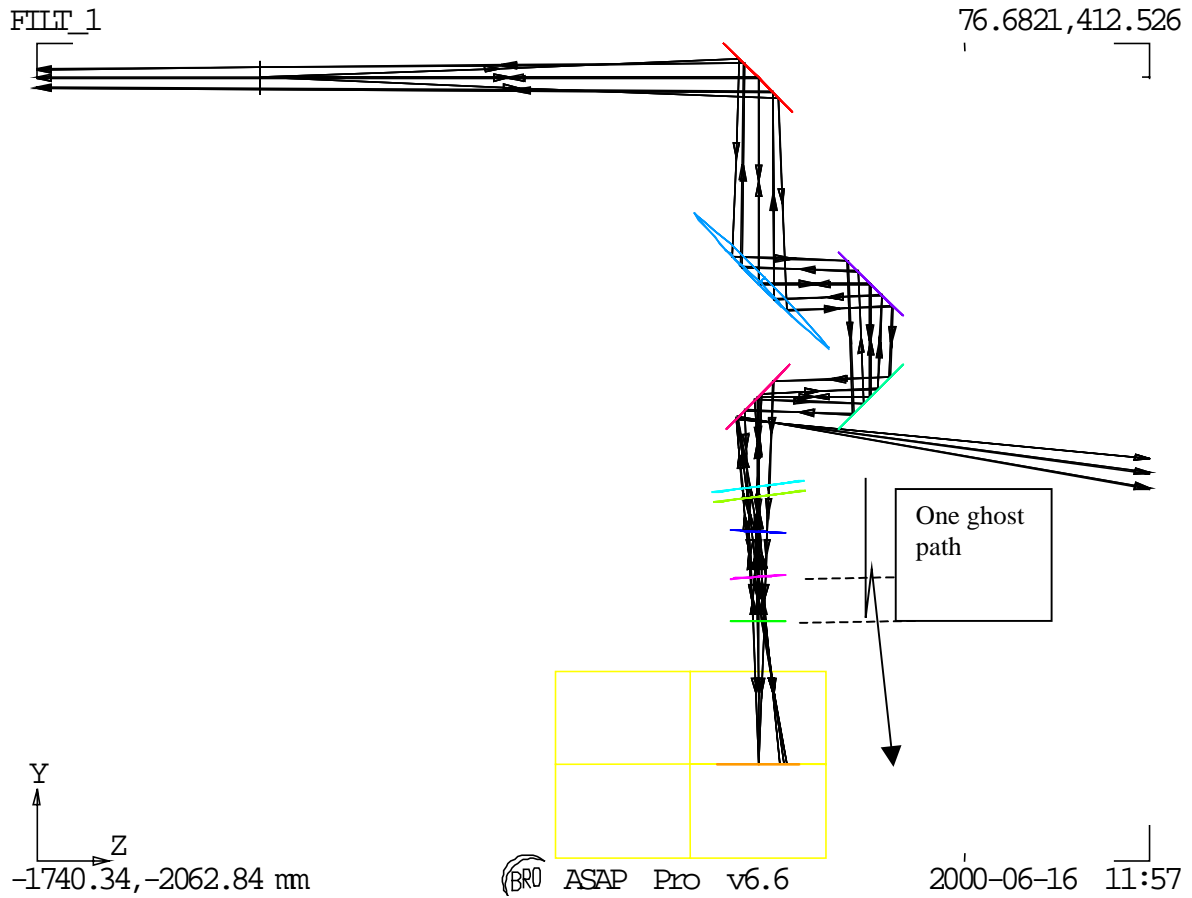
Annex 2. Filters & ghost reflections.

The figure below shows the design with 4 elements added.



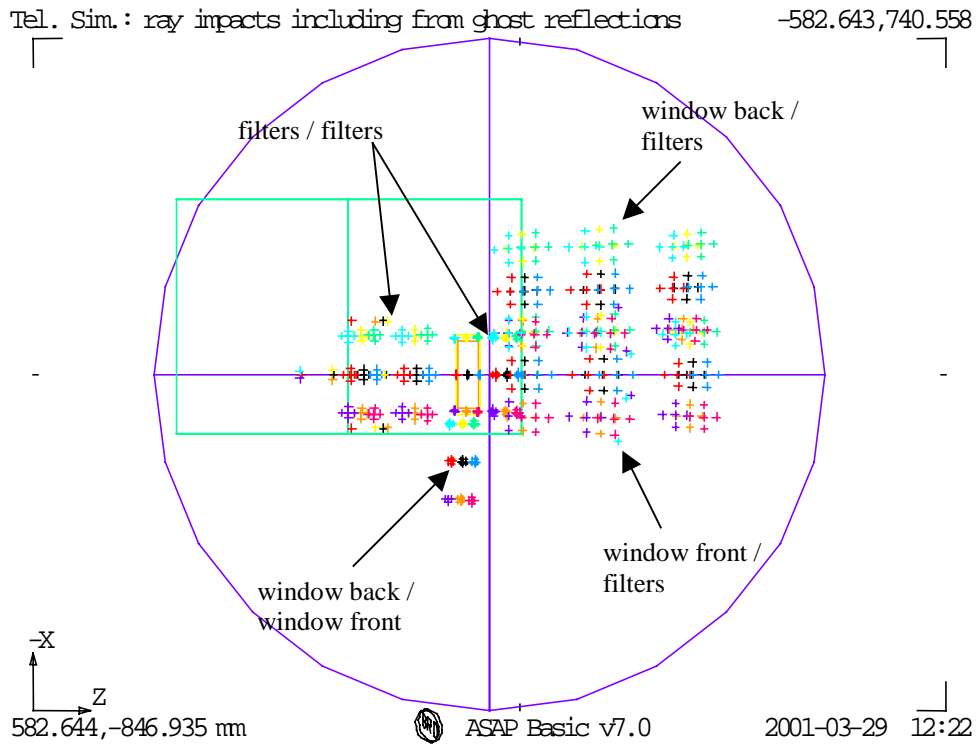
Due to the possible multiple reflections between elements, it is necessary to tilt the filters such that none of the double-bounce reflections can pass the instrument field stop. In the 1st-cut scheme shown, the elements are spaced 100mm apart (this may need to be adjusted for mechanical design). The final filter is un-tilted & the other two are tilted in opposite sense. Finally the window is tilted, by twice the amount of the filters, to prevent filter-window ghosts. The tilts are mainly about the X -axis (the inner surface of the cryostat window is also rotated about the Z-axis) so that the FOV is shifted in the direction of its narrower side (see later figure).

The figure below shows the example of a reflection between the last 2 filters, causing a defocused beam to arrive at the Field stop aperture.



NB: filter positions have been updated since this plot, see subsequent figures below.

The simplest (but perhaps overkill) arrangement is to tilt the elements such that the whole of SPIRE's FOV is shifted by its own width. In that case, for any incident beam the ghost beams are all outside of the FOV. For the 4 partly reflecting surfaces there are 5 double-bounce reflections, leading to 5 ghost images (next figure). The full ray-trace of these & resulting field-stop plane spot diagram is shown in the next figure, for the case of the new filter positions.



Here the wanted beams are those in the well-focused rectangle at the field stop. The 5 ghost reflections are defocused & are all outside of the main image as required.

This design is intended to minimise the tilt angles of the spectral filters, and uses a tilt value given by

$$\delta = \text{atan}[(2Y_0 + \text{margin}) / L_{\text{work}}'] / 2$$

where L_{work}' is the distance from last tilted filter to the field stop, and margin = 3mm here.

This gives a baseline filter tilt of 3.4 degrees (6.8 degrees for the window). Note that in this scheme there are reflections that pass back into the simulator & into the source, and the design may need to be refined to mitigate these.

New constraint from the cryostat window material and wedge angle on its front surface only (see figure below in annex 3) required a new approach. Here is the detail of the procedure:

- a window material is chosen,
- from refractive index of this material as well as window position and average thickness, the front wedge angle (back surface flat for mechanical reason) is determined to re-direct the test beam towards SPIRE aperture and input plane (beam bending to simulate the required α_4 angle),
- minimal tilt angles of the remaining filters are then determined for best ghost-reflection rejection within the cryostat path (including the defined window).

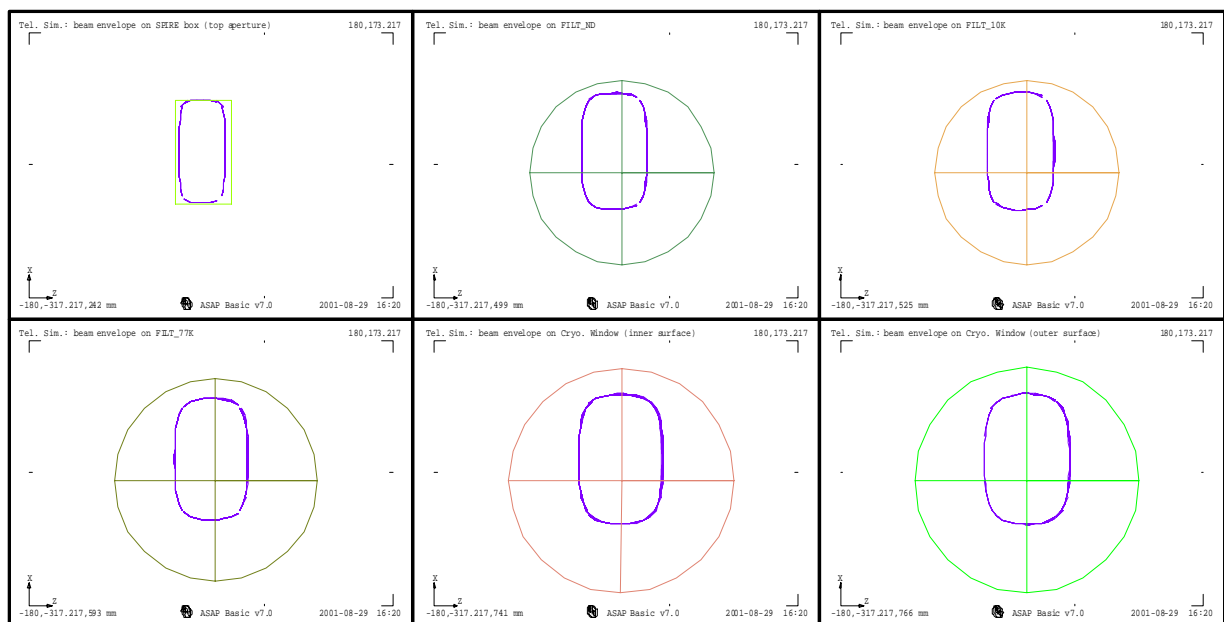
NB: all the tilts (including the window front surface) are rotation around the vertical axis (Ox) from mechanical consideration (interface within cryostat inner temperature shields along optical path). This leads to superposition of the ghost reflections from “window back/filters” and “window front/window back” with the other ones (see fig above) along the Z-axis.

The filter sizes are determined by the beam footprint (full FOV) on the different tilted filter surfaces as shown below.

Filter sizes

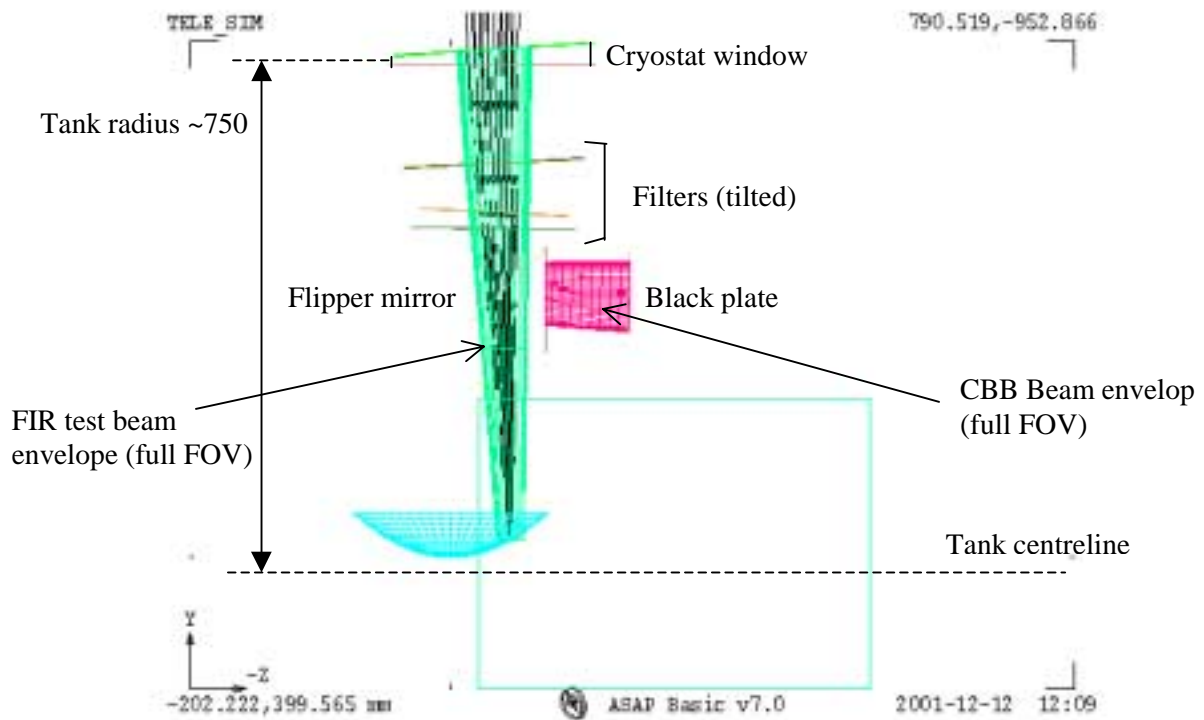
Below are displayed the beam footprints on the different surfaces (filters, cryostat window) for filters size purpose. These footprints are obtained by slicing, at these different tilted surfaces, a tube (20% oversized for diffraction), which stands as the rays envelope for all fov positions.

The diameter or linear dimensions of the superimposed surfaces is taken as *the inner diameter of the different aperture through the cryostat temperature shields*. The dimensions of the SPIRE box aperture were taken as designed in the technical note SPIRE-RAL-NOT-000694 (issue 2.01, 29/06/2001).



Annex 3. Flip mirror & cryostat black body.

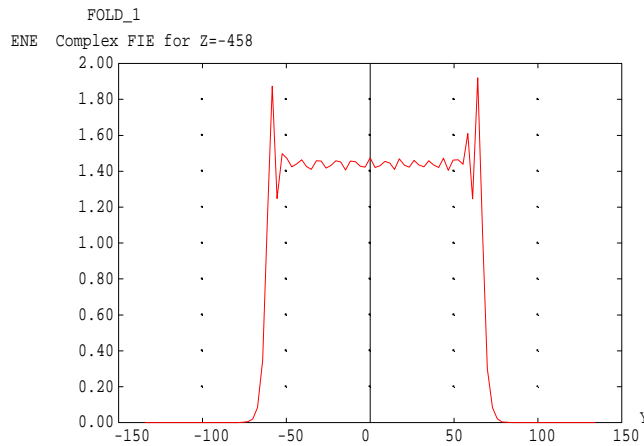
The flip mirror & black-body surface have been added to the model along with updated filter positions, and a change to make the source enter from the opposite side of the bench to previously. The updated geometry is shown in the figure below.




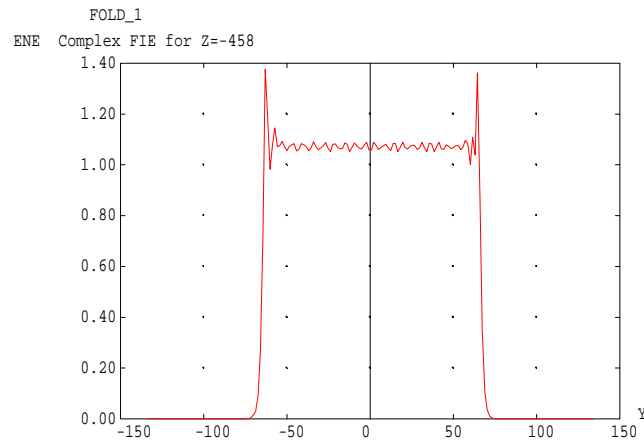
The figure shows the simulator in plan view, with the black body path flipped horizontally in Y-Z plane. The blackbody-input direction is then along the tank axis, avoiding the wall-curvature problem. Change (addition of a shutter on the top of the SPIRE box) would reduce the size of the flip mirror.


Annex 4. Beam profile due to reflective pupil mask.

In the case where a 45-degree tilted reflective pupil mask has to be considered, the beam profile in the tilted direction becomes non-ideal compared to the Herschel top-hat like profile. The tilt produces a 'ripple' at the pupil edges, to the extent shown in the simulations below.



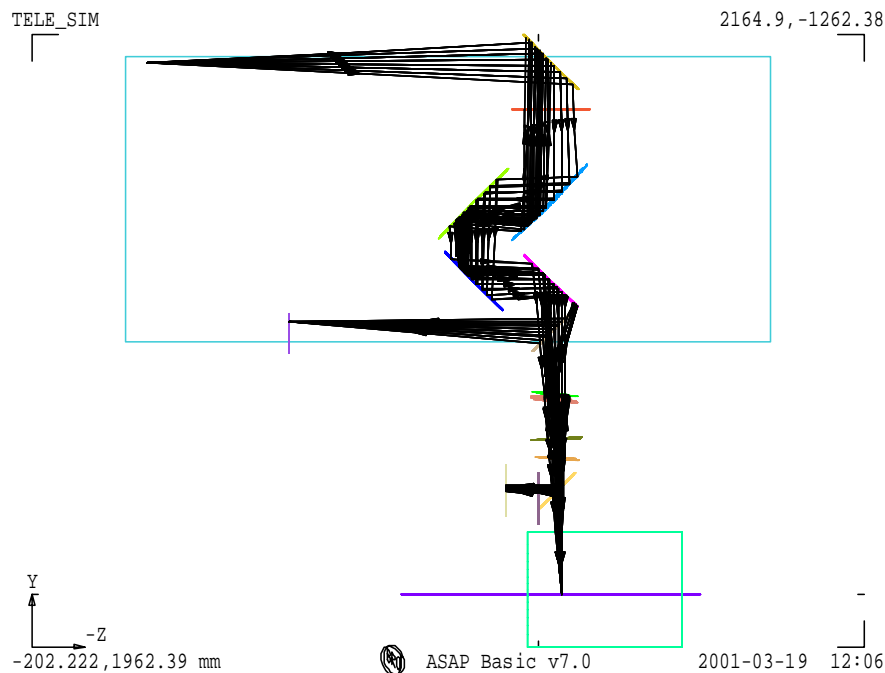
 ASAP Pro v6.6 2000-10-27 16:56
 Beam profile 0.5mm wavelength, 45 deg AOI on mask.



 ASAP Pro v6.6 2000-10-27 17:02
 AOI reduced to 20 deg.

Annex 5. Details of simulator bench layout

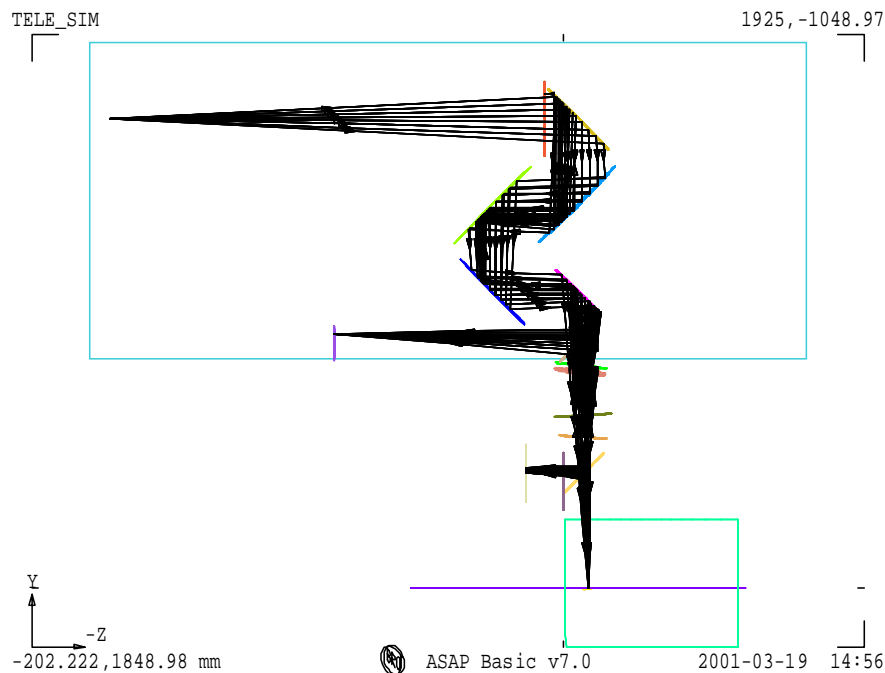
Constraint of space within the clean room test lab may lead to use of an optical bench with the following dimensions: length=2500 mm, width=1100 mm. The overall size of the telescope simulator system is set by the parameter R_{SM} . A possible configuration of the telescope simulator optical components, with $R_{SM}=2100$ mm, is displayed in the figure below (respecting the telescope F# and using a 1:1 imaging mirror and the entrance pupil mask used in transmission). It includes a beam-splitter for beam measurement check before entering the cryostat, located on the bench between F3 and the first cryostat window.



Possible layout (plan view) of the optical bench with one point-source and $R_{SM}=2100$ mm.

The dimensions of most optical components are also dependent on the R_{SM} value. Possible reduction of R_{SM} can be set thanks to reduction of the L_{WORK} distance (between F3 and the SPIRE input focal plane). An analysis (see A1 and A2) of the consequences of modification to L_{WORK} shows the needs to increase the distance between F2 and F3 (DF2F3), in order to keep the fold mirrors control laws, if L_{WORK} (as R_{SM}) is decreased. To avoid a another modification of L_{WORK} by the required increases in DF2F3, the path length from the imaging mirror M2 to F3 is chosen to be constant in every case, DF1F2 is then reduced (which helps accommodating the components along the short bench width) to compensate increasing DF2F3.

The possible source of reduction for L_{WORK} comes from the distance between the cryostat and the optical bench, limited by the requested presence of the beam-splitter. Figure 2 below shows an extreme case of reduction for R_{SM} leading to a value of 1920 mm. In order to be still able to simulate the Hershel space telescope pupil distance, the path length between the pupil aperture mask and M2 is increased (nearly linear variation, for the range of interest in R_{SM} values, with respect to decreases in DM1, the distance between the source and the mask). For this low value of R_{SM} and given the optical bench width, the beam would then need to be folded between the mask (assuming transmission mode, see Annex 4 for details of field distribution degradation in case of a reflective mask) and M2 in order to keep the mask on the bench. Such a reduction in R_{SM} (and therefore in DM1) is associated with the reduction in the pupil mask diameter D1. The parameter D1 is also set by the constraints by: $D1=n*\lambda_{max}/OSC$, where $n \gg 1$ (typically n must be larger than 10 to avoid too large diffraction effects, see R1). Taking $\lambda_{max}=0.6$ mm, and for the range of R_{SM} values studied, the parameter n varies between 25 and 35, which remains in a safe range regarding diffraction.



Possible layout (plan view) of the optical bench with one point source and $R_{SM}=1920$ mm.

Annex 6. Alternative scheme for pupil scanning.

In the case where the extra angular range needed for the mirrors prevents the above scheme from being adopted, there is an alternative scheme drawn in the figure below.

This scheme is to fold SPIRE's view through exactly 90 degrees, using a large plane mirror in the position of F3. Unlike F3 this mirror would not be scanned, and it would have to have its angle accurately referenced to the simulator system (e.g. to the bench surface, using e.g. the pentaprism method), in order that the reference of the simulator main path to SPIRE can be maintained.

The scheme would require both an angle and position control in combination. If dedicated actuators can not be provided, there is the possibility to use the existing actuators from the main path set-up (as these aren't used during this test), but this assumes that those actuators can be easily re-deployed, and it would obviously take extra time to re-configure the system in this way.

The attraction of this scheme is that the SPIRE entrance pupil is then placed in the long direction of the bench, not far from where the nominal path FIR laser beam is focused (when mirrors F1 & F2 are removed). This beam has relative aperture more than adequate for the pupil scan. The simulator focus (H) would need to be relayed to the pupil position, and a collimation + focus arrangement of 2 short-focal length paraboloids could do this. There is then also the capability to add an aperture in the collimated section whose image in the final focus mirror is placed 2.6 metres after the pupil, i.e. correctly at the SPIRE FP, (as is done also in the previous scheme). For example, a focal length of 12cm & SPIRE FP size of 100 x 30mm, this would have size $(120/2600)$ smaller, i.e. 4.6 x 1.4 mm.

The main advantage of this scheme over the preferred one is that it requires smaller angular action; the main disadvantage is that it requires re-deployment of actual actuators or else additional actuators (cf. the nominal imaging-mode set-up).

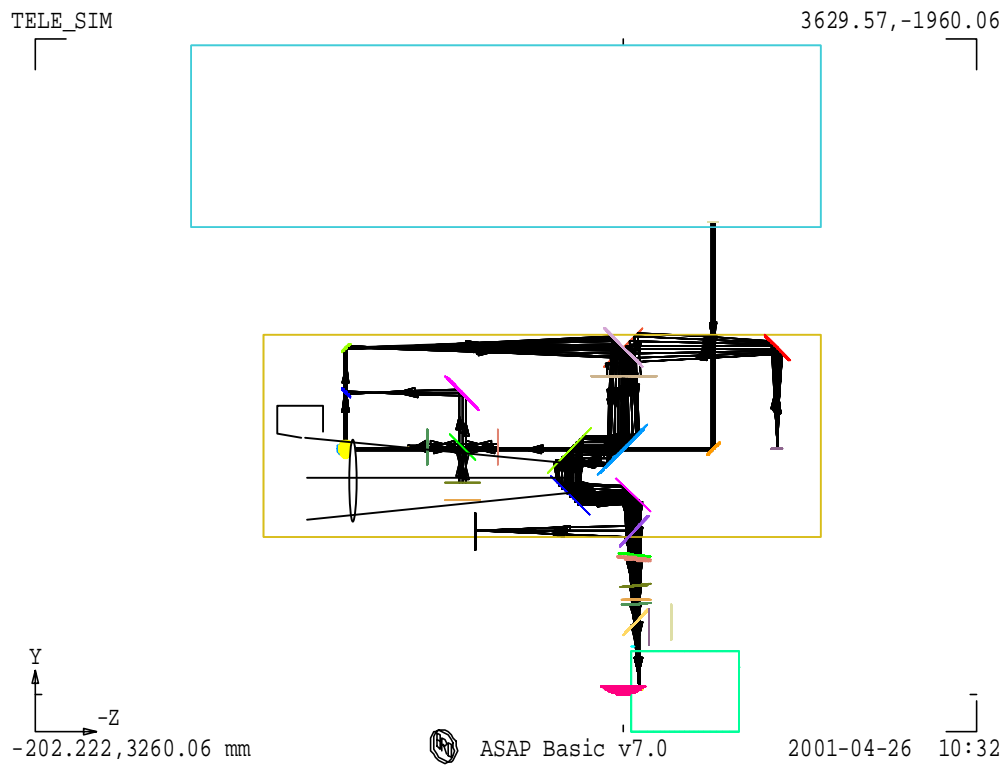


Fig. Telescope simulator layout (plan view). Possible position for the pupil to be scanned (system F1+F2 to be removed, leaving only F3 between SPIRE and the pupil).